NUMERICAL SIMULATIONS OF SURFACE ACOUSTIC WAVE-ACTUATED CELL SORTING AND ENANTIOMER SEPARATION

A Dissertation

Presented to

the Faculty of the Department of Mathematics

University of Houston

In Partial Fulfillment

of the Requirements for the Degree

Doctor of Philosophy

By

Kidist Zeleke

December 2012

NUMERICAL SIMULATIONS OF SURFACE ACOUSTIC WAVE-ACTUATED CELL SORTING AND ENANTIOMER SEPARATION

Kidist Zeleke

APPROVED:

Dr. Ronald Hoppe, Committee Chair
Department of Mathematics, University of Houston

Dr. Roland Glowinski
Department of Mathematics, University of Houston

Dr. Tsorng-Whay Pan
Department of Mathematics, University of Houston

Dr. Beatrice Riviere
Department of CAAM, Rice University

Dean, College of Natural Sciences and Mathematics

Acknowledgements

This dissertation would not have been possible without the guidance and the help of several individuals who in one way or another contributed in the completion of my study.

My utmost gratitude goes to my advisor Dr. Ronald Hoppe without whom none of this would have been possible. I would like to thank him for introducing me to this exciting field of computational PDEs, for funding my research and his unreserved help and kindness whenever I needed it.

I like to acknowledge Christopher Linsenmann for letting me use his IB package and Harbir Antil, for his encouragement, mentorship and guidance specially in the early stages of my study.

Last but not least, I would like to thank all my friends who made my stay in Houston incredible and my family for honoring my decisions and letting me do what I desired.

This dissertation is dedicated to Tensay Bekele and Terefe Zeleke.

NUMERICAL SIMULATIONS OF SURFACE ACOUSTIC WAVE-ACTUATED CELL SORTING AND ENANTIOMER SEPARATION

An Abstract of a Dissertation

Presented to

the Faculty of the Department of Mathematics

University of Houston

In Partial Fulfillment

of the Requirements for the Degree

Doctor of Philosophy

By

Kidist Zeleke

December 2012

Abstract

This dissertation is focused on the mathematical modeling and numerical simulations of cell sorting and enatiomer separation using surface acoustic wave-actuated fluid flow.

We model a high throughput sorting of two different types of biological cells (type I and type II) by a biomedical micro-electro-mechanical system (BioMEMS) whose operating principle depends on surface acoustic wave (SAW)-manipulated fluid flow in a microchannel. The BioMEMS consists of a separation channel with three inflow channels for injection of the carrier fluid and the cells, two outflow channels for separation, and an interdigital transducer (IDT) close to the lateral wall of the separation channel for generation of the SAWs. The cells can be distinguished by fluorescence. The inflow velocities are tuned such that, without SAW actuation, a cell of type I leaves the device through a designated outflow channel. However, if a cell of type II is detected, the IDT is switched on and the SAWs modify the fluid flow such that the cell leaves the separation channel through the other outflow boundary.

Enantiomers are chiral objects such as chemical molecules that can be distinguished by their handedness. They typically occur as racemic compounds of left- and right-handed species which may have completely different properties. Therefore, in applications such as drug design in pharmacology, enantiomer separation is an important issue. In this dissertation, we present a new technology for enantiomer separation by surface acoustic wave generated vorticity patterns consisting of pairwise counter-rotating vortices in a carrier fluid. The enantiomers are injected onto the surface of the fluid between two counter-rotating vortices such that right-handed

(left-handed) enantiomers are attracted by left-rotating (right-rotating) vortices.

For modeling and numerical simulation of the cell sorting and enantiomer separation process we use the Finite Element Immersed Boundary (FE-IB) method, which relies on the solution of a coupled system consisting of the incompressible Navier-Stokes equations, and the equations of motion of the immersed structures described with respect to an Eulerian and a Lagrangian coordinate system.

The results of the numerical simulation are compared with experimentally obtained results [20, 10], and they are in excellent agreement.

Key words: cell sorting, enantiomer separation, surface acoustic waves, finite element immersed boundary method

Contents

List of Figures

List of Tables

CHAPTER 1

Introduction

Biomedical Micro-Electro-Mechanical Systems (BioMEMS) are miniaturized laboratories on a chip (lab-on-a-chip) that can be used for various biomedical and biochemical purposes such as hybridization in genomics, protein profiling in proteomics, and cytometry in cell analysis. In the past two decades, research on miniaturized labs has seen enormous development, mainly due to the need to reduce costs by reducing the consumption of expensive reagents and by increasing throughput and automation. On the other hand, the ability to sort particles in a sample has been a critical need with constantly expanding areas of application. Thus, the revolution of lab-on-a chip with the investigation of continuous flow separation methods, has played a significant

role in advancing designs of microfluidic separation devices [37].

Many new ideas of how to manipulate small amounts of fluids and particles therein have been suggested. Recently, it has been shown that the agitation of fluids by surface acoustic waves (SAWs) on piezoelectric substrates presents a versatile method of manipulating and controlling the flow of small amounts of a fluid [31].

In this work we are concerned with a high throughput cell sorting and enantiomer separation using surface acoustic wave-manipulated fluid in microchannels which have significant applications in basic cell biology, cancer research, clinical diagnostics, pharmaceutical manufacturing, and selection of rare multicellular events [12, 15, 28, 43, 45].

Modern cell sorting schemes operate in two different ways: Cells are either sorted in continuous flow or encapsulated in small liquid droplets prior to sorting. When sorting in continuous flow, one has to deal with low contrast of material properties of cells and the bulk media because both are typically aqueous liquids. To overcome this limitation, responsive beads are often biochemically attached to the cells to enhance the separation efficiency. But these techniques suffer from slow response time and consequently slow sorting rates. In the latter case, the problem of sorting applies to the droplets and not to the cells. Drops can be sorted in air or in another immiscible continuous liquid. Traditional fluorescence activated cell sorters encapsulate cells in drops in air which are then labeled with an electric charge and subsequently separated in an electric field. These sorters reach very high sorting rates but have several disadvantages among others, large dead volume which makes it impossible to separate cells from small sample volumes. Another technique is to employ standing

surface acoustic waves (SSAW) which can be used to align and wash particles. In SSAW, a stationary standing wave is built up and objects are driven to positions of larger or smaller wave amplitude according to their compressibility contrast with respect to the suspending medium. This force is often called acoustic radiation force and is induced by an ultrasonic standing wave field. Acoustic radiation force acting on an interface between two liquids with different densities can also be used to actuate the heterogeneous fluid itself [20].

All the methodologies mentioned before heavily rely on different properties of the cells in the sample (density/size, charge/polarization, magnetic labeling) and hence are restricted to specific applications. A recent trend is to use surface acoustic wave actuated fluid flow for cell-sorting (SAWACS) [20]. In this device, the homogeneous continuous fluid is actuated including the objects and no contrast in compressibility, dielectric constant or density is required. This scheme combines many advantages of fluorescence-activated cell sorting (FACS) and fluorescence-activated droplet sorting (FADS) in microfluidic channels. Cells are directed by acoustic streaming excited by a surface acoustic wave which deflects the fluid independently of the contrast in the material properties of the deflected objects and the continuous phase; thus the device's underlying principle works without additional enhancement of the sorting by prior labeling of the cells with responsive markers such as magnetic or polarizable beads. Single cells are sorted directly from bulk media at rates as fast as several kHz without prior encapsulation into liquid droplet compartments as in traditional FACS [20].

A geometric object is called chiral, if it is not identical to its mirror image, and

achiral, otherwise. A chiral object and its mirror image are called enantiomers (or stereoisomers, optical isomers). Since the chemical synthesis of enantiomers usually gives rise to racemic compounds, i.e., compounds consisting of the same amount of left-and right-handed species, enantiomer separation plays a significant role in agrochemical, electronic, and pharmaceutical as well as food flavor and fragrance industries (cf., e.g., [4, 13, 14, 19, 32, 38]).

The main established methods of enantiomer separation are gas or liquid chromatography and capillary electrophoresis [31]. In both cases specific chiral filling materials are used to obtain different elusion times of the enantiomers. Moreover, long columns are needed through which the enantiomers are dragged by a large pressure or a high voltage difference. Chemically less specific methods that work with less substance and that do not require high voltages or pressure would be of great advantage.

Recently, it has been shown that SAWs can be used to generate specific flow patterns in the carrier fluid such as vorticity patterns consisting of mutually counter-rotating vortices. Since enantiomers drift in microflows with a direction depending on their chirality (cf., e.g., [11, 31, 34, 36]), SAW-induced vorticity patterns can be exploited for enantiomer separation in racemic compounds in the sense that particles with a given chirality primarily accumulate in vortices of the same direction of rotation, whereas their chiral counterparts accumulate in vortices which are counter-rotating.

In this dissertation, we present mathematical models and numerical simulations

for surface acoustic wave-actuated cell sorting and separation of deformable vesicle-like enantiomers. For this purpose, the finite element immersed boundary method (FE-IB) is used. This method is a variation of the immersed boundary (IB) method which was originally proposed by Peskin for modeling and simulation of blood flow patterns around heart valves. The IB method is known to be a powerful tool, applicable to general fluid-structure interaction problems involving incompressible viscous fluid containing an immersed elastic interface [40, 41].

The dissertation is organized as follows: in the second chapter, we introduce the immersed boundary method. We discuss the formulation of the original immersed boundary (IB) method and the finite element immersed boundary method (FE-IB) briefly.

Chapter three is devoted to the presentation of surface acoustic wave-actuated cell sorting (SAWACS). We provide the mathematical model and stability estimates for both continuous and discrete problems. Finally, we provide results of numerical simulations for the sorting of a red blood cell and malignant breast cancer cell that will prove the feasibility of SAWACS.

In chapter four, we study the separation of vesicle-like deformable L-shaped enantiomers by SAWs. We discuss the experimental set up, mathematical model, and numerical results. We will further compare our results of numerical simulation with experimentally obtained results and with other current simulations done for rigid L-shaped enantiomers.

And finally, we conclude the dissertation by discussing future work directions in

the fifth chapter.

CHAPTER 2

An Introduction to the Immersed Boundary Method

In this chapter, we provide a brief introduction to the Immersed Boundary (IB) method which is a frequently used tool for the mathematical modeling and numerical simulation of fluid-structure interaction problems, especially in biological fluid dynamics.

The IB method was originally introduced by Charles Peskin to study flow patterns around heart valves in 1972 [39]. Since then it has been applied to a wide range of problems, including platelet aggregation during blood clotting [17], fluid dynamics of the inner ear [5], flow of suspensions [18], aquatic animal locomotion [16], and flow in collapsible tubes [42]. The mathematical formulation uses Eulerian

variables for the modeling of the fluid motion and Lagrangian variables for the immersed structure which are related by interaction equations. We refer to the survey article [41] for details and further references. In the original formulation, the Dirac delta function plays an important role and the finite difference method is used for the spatial discretization of the problem. Later, D. Boffi et al. [8, 9, 7] provided a variational formulation of these equations in such a way that the Dirac delta function is not directly involved and the finite element method is used for spatial discretization. This extension of the IB method is referred to as the Finite Element Immersed Boundary (FE-IB) method.

2.1 Notation and function spaces

Throughout this chapter and the rest of the dissertation, we will use standard notation from Lebesgue and Sobolev space theory (cf., e.g., [46]). In particular, for a bounded polygonal domain $\Omega \subset \mathbb{R}^2$ with boundary $\Gamma = \partial\Omega$, we denote by $L^2(\Omega)$ and $\mathbf{L}^2(\Omega)$ the Hilbert spaces of scalar and vector-valued Lebesgue integrable functions on Ω with inner products $(\cdot,\cdot)_{0,\Omega}$ and norms $\|\cdot\|_{0,\Omega}$ respectively. We refer to $L^2_0(\Omega)$ as the subspace of functions with zero integral mean. Further, we denote by $H^s(\Omega)$ and $\mathbf{H}^s(\Omega), s \in \mathbb{R}_+$, the Sobolev spaces of scalar and vector-valued functions with inner products $(\cdot,\cdot)_{s,\Omega}$ and associated norms $\|\cdot\|_{s,\Omega}$. For $\Gamma' \subset \Gamma$, the spaces $H^s_{0,\Gamma'}(\Omega)$ and $\mathbf{H}^s_{0,\Gamma'}(\Omega)$ are the closures of $C^\infty_{0,\Gamma'}(\Omega)$ and $\mathbf{C}^\infty_{0,\Gamma'}(\Omega)$ in $H^1(\Omega)$ and $\mathbf{H}^1(\Omega)$. We will omit the subindex Γ' in case $\Gamma' = \Gamma$ and we denote $C^\infty_0(\Omega)$ resp. $\mathbf{C}^\infty_0(\Omega)$ by $\mathcal{D}$ resp. $\boldsymbol{\mathcal{D}}$. The spaces $H^{-s}(\Omega)$ and $\mathbf{H}^{-s}(\Omega)$ stand for the dual spaces of $H^s_0(\Omega)$

and $\mathbf{H}_0^s(\Omega)$ with $\langle\cdot,\cdot\rangle_{H^{-s},H_0^s}$ and $\langle\cdot,\cdot\rangle_{\mathbf{H}^{-s},\mathbf{H}_0^s}$ referring to the dual products. Likewise, for closed subspaces $V \subset H^1(\Omega)$ and $\mathbf{V} \subset \mathbf{H}^1(\Omega)$ the spaces V^* and $\mathbf{V}^*$ denote the dual spaces and $\langle\cdot,\cdot\rangle_{V^*,V}$ and $\langle\cdot,\cdot\rangle_{\mathbf{V}^*,\mathbf{V}}$ are the associated dual products. The spaces $H^s(\bar{\Omega}) \subset H^s(\Omega)$ and $\mathbf{H}^s(\bar{\Omega}) \subset \mathbf{H}^s(\Omega)$ are the subspaces of all functions $u|_\Omega$ and $\mathbf{u}|_\Omega$ where $u \in H^s(\mathbb{R}^d)$ and $\mathbf{u} \in \mathbf{H}^s(\mathbb{R}^d)$ such that $\langle u|_\Omega, \varphi\rangle = \langle u, \tilde{\varphi}\rangle$ and $\langle \mathbf{u}|_\Omega, \boldsymbol{\varphi}\rangle = \langle \mathbf{u}, \tilde{\boldsymbol{\varphi}}\rangle$ for all $\varphi \in C_0^\infty(\Omega)$ and $\boldsymbol{\varphi} \in \mathbf{C}_0^\infty(\Omega)$ with $\tilde{\varphi}$ and $\tilde{\boldsymbol{\varphi}}$ referring to the continuation of φ and $\boldsymbol{\varphi}$ by zero outside Ω. For $\Gamma' \subset \Gamma$, we denote by $H^{s-1/2}(\Gamma')$ and $\mathbf{H}^{s-1/2}(\Gamma')$, $s \geq 1$, the trace space of scalar and vector-valued functions in $H^s(\Omega)$ and $\mathbf{H}^s(\Omega)$ on Γ'. We further refer to $H_{00}^{s-1/2}(\Gamma')$ and $\mathbf{H}_{00}^{s-1/2}(\Gamma')$ as the spaces of functions whose extensions by zero to $\Gamma \setminus \Gamma'$ belong to $H^{s-1/2}(\Gamma)$ and $\mathbf{H}^{s-1/2}(\Gamma)$. Finally, we denote by $C^{k,\mu}(\Omega)$ and $\mathbf{C}^{k,\mu}(\Omega)$, $k \in \mathbb{N}_0, \mu \in (0, 1/2)$, the Banach spaces of k-times continuously differentiable scalar and vector-valued functions on Ω whose derivatives of order k are Hölder continuous of order μ.

Moreover, for $T > 0$ and a Banach space Z ($\mathbf{Z}$) of scalar (vector-valued) functions, we denote by $L^2((0,T),Z)$ ($\mathbf{L}^2((0,T),\mathbf{Z})$) the Hilbert space and by $C([0,T],Z)$ ($\mathbf{C}([0,T],\mathbf{Z})$) the Banach space of functions $v : [0,T] \to Z$ ($\mathbf{v} : [0,T] \to \mathbf{Z}$) with norms

$$\|v\|_{L^2((0,T),Z)} := \Big(\int_0^T \|v(t)\|_Z^2 dt \Big)^{1/2},$$

$$\|v\|_{C([0,T],Z)} := \max_{t\in[0,T]} \|v(t)\|_Z,$$

and analogous settings in the vector-valued case. The spaces $H^s((0,T),Z)$, $s \in \mathbb{R}_+$, ($\mathbf{H}^s((0,T),\mathbf{Z})$) are defined likewise. Further notations can be found in Appendix B.

2.2 The classical immersed boundary method

The IB method is a mixed Euler-Lagrangian finite-difference method for computing the flow interaction with a flexible immersed boundary. In this method the fluid flow is governed by the incompressible Navier-Stokes equations and these are solved on a stationary Cartesian grid. The immersed body is represented by a set of massless elastic fibers and the location of these fibers is tracked in a Lagrangian manner by a collection of massless points that move with the local fluid velocity. The force density is defined by a delta function layer that represents the force applied by the immersed boundary to the fluid. Since the location of the fibers does not generally coincide with the nodal points of the Cartesian grid, the forcing is distributed over a band of cells around each Lagrangian point (cf. Figure 2.1) and this distributed force will be used in the momentum equations.

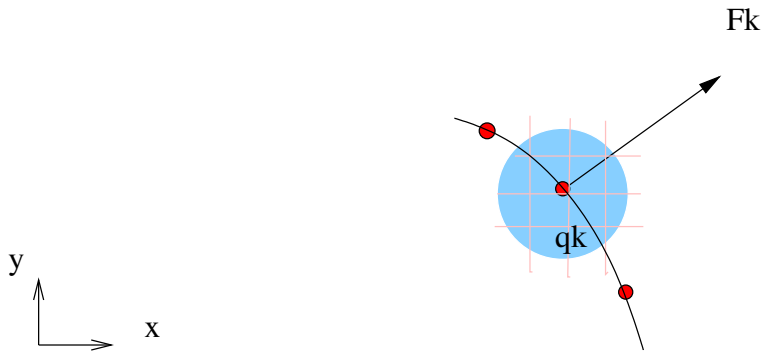

Figure 2.1: Transfer of force from Lagrangian boundary point to surrounding fluid nodes.

Therefore, the general structure of the immersed boundary method is based on three types of equations:

1. the incompressible Navier-Stokes equations for the description of the fluid,
2. the elasticity equations describing the total elastic force exerted by the immersed body,
3. the interaction equations to translate Lagrangian into Eulerian coordinates and vice versa.

2.2.1 The incompressible Navier-Stokes equations

The Navier-Stokes equations describe the dynamics of a viscous incompressible Newtonian fluid with respect to the Eulerian variables denoted by $\mathbf{x}$:

$$\rho_f(\frac{\partial \mathbf{v}}{\partial t} + \mathbf{v} \cdot \nabla \mathbf{v}) - \nabla \cdot \boldsymbol{\sigma} = \mathbf{f} \quad \text{in } \Omega \times (0,T) \tag{2.1a}$$

$$\nabla \cdot \mathbf{v} = 0 \quad \text{in } \Omega \times (0,T) \tag{2.1b}$$

$$\mathbf{v} = \mathbf{v}_D \quad \text{on } \partial\Omega_D \times (0,T) \tag{2.1c}$$

$$\boldsymbol{\sigma}(\mathbf{v},p)\mathbf{n} = \mathbf{0} \quad \text{on } \partial\Omega_N \times (0,T) \tag{2.1d}$$

$$\mathbf{v}(\cdot,0) = \mathbf{v}_0 \quad \text{in } \Omega \tag{2.1e}$$

Here, ρ_f denotes the density of the fluid. The unknowns $\mathbf{v}(\mathbf{x},t)$ and $p(\mathbf{x},t)$ represent the velocity and the pressure, respectively. $\mathbf{f}$ denotes the density of a body force acting on the fluid. It usually contains a singular vector field which is zero everywhere except possibly on the curve representing the boundary of the immersed structure. $\Delta\mathbf{v}$ has to be understood componentwise with components $\Delta\mathbf{v}_i$, and similarly the

convection terms $\mathbf{v}\cdot\nabla\mathbf{v} = (\mathbf{v}\cdot\nabla\mathbf{v})_{i=1}^{d}$ with $(\mathbf{v}\cdot\nabla\mathbf{v})_i := \Sigma_{j=1}^{d}\mathbf{v}_j\frac{\partial\mathbf{v}_i}{\partial x_j}$. Further, $\sigma(\mathbf{v},p) = -pI_d + 2\eta\varepsilon(\mathbf{v})$ is the *stress tensor* , where $\varepsilon(\mathbf{v}) = 1/2(\nabla\mathbf{v} + (\nabla\mathbf{v})^T)$ is called the *rate of strain tensor* or *rate of deformation tensor* and η is the dynamic viscosity of the fluid. Throughout this thesis, ρ_f and η are taken to be constant.

Equation (2.1a) describes the conservation of momentum and (2.1b) is the incompressibility condition for the fluid. The equations (2.1c) and (2.1d) are the Dirichlet and the Neumann (" do-nothing") boundary conditions with $\overline{\partial\Omega_D}\cup\overline{\partial\Omega_N} = \partial\Omega$ and $\partial\Omega_D\cap\Omega_N = \emptyset$, where typically $\partial\Omega_N$ is the outflow part of the boundary. The function $\mathbf{v}_D$ in (2.1c) describes a prescribed velocity and $\mathbf{n}$ in (2.1d) is the exterior unit normal on $\partial\Omega_N$. Finally, the function $\mathbf{v}_0$ in (2.1e) is a given initial velocity.

Remark 2.2.1. For the rest of this chapter, we assume $\mathbf{v}_D = \mathbf{0}$ in (2.1c). This can be done without loss of generality, because otherwise we define $\tilde{\mathbf{v}}$ as the solution of (2.1a)-(2.1e) with $\mathbf{f} = \mathbf{0}$ in (2.1a) and $\mathbf{v}|_{\partial\Omega_D} = \mathbf{v}_D$. Then, $\hat{\mathbf{v}} := \mathbf{v} - \tilde{\mathbf{v}}$ satisfies (2.1a)-(2.1e) with $\hat{\mathbf{v}}_D = \mathbf{0}$ in (2.1c).

2.2.2 Material elasticity equations

In this subsection, we describe the mathematical model for the total force exerted on the carrier fluid by the immersed structure. The immersed bodies are considered to be elastic materials occupying subdomains $B_t^{(i)} \subset \Omega, 1 \le i \le N,\ t \in [0,T]$, with boundaries $\partial B_t^{(i)}$ which are non-self-intersecting closed curves or surfaces such that $\partial B_t^{(i)} \cap \partial B_t^{(j)} = \emptyset,\ 1 \le i \ne j \le N$. For simplicity we consider $N = 1$ and write B_t and ∂B_t instead of B_t^1 and $\partial B_t^{(1)}$ in our discussion. The generalization to $N > 1$ is

straightforward. We also assume that L is the length of the boundary of the initial configuration, i.e., $L = |\partial B_0|$.

Let $\bar{q} \in [0, L]$ be the coordinate labeling a material point on ∂B_0. We denote the position of that point in Ω at time t by $\mathbf{X}(\bar{q}, t)$. We further denote by $\varepsilon_e(\mathbf{X}(\bar{q}, t))$ and $\varepsilon_b(\mathbf{X}(\bar{q}, t))$ the local energy densities on the elastic boundary ∂B_t. The associated bending and elastic energies are given by

$$E_e(t) =: \int_0^L \varepsilon_e(\mathbf{X}(\bar{q}, t)) d\bar{q}, \tag{2.2a}$$

$$E_b(t) =: \int_0^L \varepsilon_b(\mathbf{X}(\bar{q}, t)) \bar{q}, \tag{2.2b}$$

such that the total energy reads:

$$E(t) := E_e(t) + E_b(t), \ t \in (0, T). \tag{2.3}$$

Using the principle of virtual work, the local force density $\mathbf{F}$ is given by the Gâteaux derivative of E according to

$$\mathbf{F}(\bar{q}, t) = -E'(\mathbf{X}(\bar{q}, t)) \tag{2.4}$$

2.2.3 Interaction equations

The most outstanding feature of the immersed boundary method is that the immersed bodies are considered to be part of the fluid. This is done using interaction equations that couple the elasticity equations with the fluid equations.

In general, the mass density of the immersed body can be described by introducing an excess Lagrangian mass density $M(\bar{q})$, i.e., the difference between the mass of the immersed body and the mass of the fluid displaced by it. Then, we can express the density of the fluid , $\bar{\rho}$, in terms of $M(\bar{q})$. Assuming $\mathbf{F}(\cdot, t) \in \mathbf{C}(\partial B_t)$, the interaction equations are given by

$$\mathbf{f}(\mathbf{x}, t) = \int_0^L \mathbf{F}(\bar{q}, t)\boldsymbol{\delta}(\mathbf{x} - \mathbf{X}(\bar{q}, t))d\bar{q}, \qquad \text{in } \Omega \times (0, T) \tag{2.5a}$$

$$\bar{\rho}(\mathbf{x}, t) = \rho_f + \int_0^L M(\bar{q})\boldsymbol{\delta}(\mathbf{x} - \mathbf{X}(\bar{q}, t))d\bar{q}, \qquad \text{in } \Omega \times (0, T) \tag{2.5b}$$

where $\boldsymbol{\delta}$ is the Dirac delta function in $\mathbb{R}^d$. The force density $\mathbf{f}$ is the right-hand side of (2.1a) and describes the interaction between the fluid and the immersed body. Here, we observe that $\mathbf{F}$ takes into account the elasticity properties of the immersed structure while $\mathbf{f}$ is purely in the Eulerian framework.

Remark 2.2.2. Throughout the thesis, we assume that the immersed boundary is massless, i.e, $M = 0$. Hence, equation (2.5b) will not be used in subsequent discussions.

In order to compute the position of the immersed body, we use the following relation:

$$\begin{aligned} \frac{\partial \mathbf{X}}{\partial t}(\bar{q}, t) &= \int_\Omega \mathbf{v}(\mathbf{x}, t)\boldsymbol{\delta}(\mathbf{x} - \mathbf{X}(\bar{q}, t))d\mathbf{x} \\ &= \mathbf{v}(\mathbf{X}(\bar{q}, t), t), \quad \text{in } \Omega \times (0, T), \end{aligned} \tag{2.6}$$

where $\mathbf{v}(\cdot, t) \in \mathbf{C}(\Omega)$ for $t \in (0, T]$. The equation (2.6) enforces the no slip condition for viscous fluid, i.e., the immersed body moves at the same velocity as the fluid.

2.2.4 The immersed boundary system

In summary, the equations of motion for the fluid-structure system is to find $\mathbf{v}$, p and $\mathbf{X}$ satisfying:

$$\rho_f(\frac{\partial \mathbf{v}}{\partial t} + \mathbf{v}\cdot\nabla\mathbf{v}) - \mu\Delta u + \nabla p = \mathbf{f} \quad \text{in } \Omega\times(0,T), \tag{2.7a}$$

$$\nabla\cdot\mathbf{v} = 0 \quad \text{in } \Omega\times(0,T), \tag{2.7b}$$

$$\mathbf{f}(\mathbf{x},t) = \int_0^L \mathbf{F}(\bar{q},t)\boldsymbol{\delta}(\mathbf{x}-\mathbf{X}(\bar{q},t))d\bar{q} \quad \text{in } \Omega\times(0,T), \tag{2.7c}$$

$$\frac{\partial \mathbf{X}}{\partial t}(\bar{q},t) = \mathbf{v}(\mathbf{X}(\bar{q},t),t) \quad \text{in } \partial B_t\times(0,T), \tag{2.7d}$$

$$\mathbf{v} = \mathbf{0} \quad \text{on } \partial\Omega_D\times(0,T), \tag{2.7e}$$

$$\boldsymbol{\sigma}(\mathbf{v},p)\mathbf{n} = \mathbf{0} \quad \text{on } \partial\Omega_N\times(0,T), \tag{2.7f}$$

$$\mathbf{v}(\cdot,0) = \mathbf{v}_0 \quad \text{in } \Omega, \tag{2.7g}$$

$$\mathbf{X}(\bar{q},0) = \mathbf{X}_0(\bar{q}) \quad \text{in } B_0, \tag{2.7h}$$

where $\mathbf{X}_0$ is the position of the initial configuration of the immersed boundary.

2.3 The variational formulation of the immersed boundary method

In the original immersed boundary method, the spatial discretization is done using the finite difference approach. The main concern is the computation of $\mathbf{f}$ in (2.5a) due to the presence of the Dirac delta function. This has been realized by constructing an appropriate approximation $\boldsymbol{\delta}_h$ for $\boldsymbol{\delta}$ which is nonsingular for each h and approaches $\boldsymbol{\delta}$ as $h \to 0$ (cf. [7, 41]).

In this work, we use the finite element approach for the spatial discretization of the fluid equations and periodic cubic splines for the immersed boundary. The force term involving the Dirac delta function is dealt with in a variational way, so there is no need for an approximation of $\boldsymbol{\delta}$. To this end, we need to introduce the variational formulation of the immersed boundary equations (2.7) and this will be the purpose of this section. Setting $\mathbf{V} := \mathbf{H}^1_{0,\partial\Omega_D}(\Omega)$, the following result from [7] allows the interpretation of the force density $\mathbf{f}(t),\ t \in (0,T)$, as a distribution in $\mathbf{V}^*$.

Lemma 2.3.1. *Assume that for all $t \in [0,T]$, the immersed boundary ∂B_t is Lipschitz continuous. Then, for all $t \in (0,T)$ the force density $\mathbf{f}(t)$ is a distribution in $\mathbf{V}^*$ defined according to*

$$\langle \mathbf{f}(t), \mathbf{w} \rangle_{\mathbf{V}^*,\mathbf{V}} = \int_0^L \mathbf{F}(\bar{q},t) \cdot \mathbf{w}(\mathbf{X}(\bar{q},t)) d\bar{q}, \quad t \in (0,T),\ \mathbf{w} \in \mathbf{V}. \tag{2.8}$$

Proof. Denoting by $B_\varepsilon(0)$ the ball with center 0 and radius $\varepsilon > 0$, we consider the family of continuous functions $\delta_\varepsilon > 0$ such that

$$\text{supp}(\delta_\epsilon) \subseteq \mathcal{B}_\epsilon(0), \quad \int_{\mathcal{B}_\epsilon(0)} \delta_\epsilon \, d\mathbf{x} = 1, \ \delta_\epsilon \to \delta \text{ in } \boldsymbol{\mathcal{D}}', \text{ as } \epsilon \to 0. \tag{2.9}$$

Setting

$$\mathbf{f}_\epsilon(\mathbf{x}, t) = \int_0^L \mathbf{F}(q,t)\delta_\epsilon(\mathbf{x} - \mathbf{X}(q,t)) \, dq \quad \forall \mathbf{x} \in \Omega, \ t \in (0,T),$$

for $\mathbf{w} \in \boldsymbol{\mathcal{D}}(\Omega) := \mathbf{C}^\infty_{0,\partial\Omega_D}(\Omega)$, Fubini's theorem yields

$$\begin{aligned}
\langle \mathbf{f}_\varepsilon(t), \mathbf{w} \rangle_{\boldsymbol{\mathcal{D}}',\boldsymbol{\mathcal{D}}} &= \int_\Omega \mathbf{f}_\varepsilon(\mathbf{x},t) \cdot \mathbf{w}(\mathbf{x}) \, d\mathbf{x} \\
&= \int_\Omega \left(\int_0^L \mathbf{F}(q,t)\delta_\epsilon(\mathbf{x} - \mathbf{X}(q,t)) \, dq \right) \cdot \mathbf{w}(\mathbf{x}) \, d\mathbf{x} \\
&= \int_0^L \mathbf{F}(q,t) \left(\int_\Omega \delta_\epsilon(\mathbf{x} - \mathbf{X}(q,t)) \cdot \mathbf{w}(\mathbf{x}) \right) \, d\mathbf{x} \, dq.
\end{aligned} \tag{2.10}$$

Using (2.9) and passing to the limit by interchanging the order of the limit and the integration, we obtain

$$\begin{aligned}
\langle \mathbf{f}(t), \mathbf{w} \rangle_{\boldsymbol{\mathcal{D}}',\boldsymbol{\mathcal{D}}} &= \lim_{\varepsilon \to 0} \langle \mathbf{f}_\varepsilon(t), \mathbf{w} \rangle_{\boldsymbol{\mathcal{D}}',\boldsymbol{\mathcal{D}}} \\
&= \lim_{\varepsilon \to 0} \int_0^L \mathbf{F}(q,t) \left(\int_\Omega \delta_\varepsilon(\mathbf{x} - \mathbf{X}(q,t)) \cdot \mathbf{w}(\mathbf{x}) \right) \, d\mathbf{x} \, dq \\
&= \int_0^L \mathbf{F}(q,t) \left(\lim_{\epsilon \to 0} \int_\Omega \delta_\epsilon(\mathbf{x} - \mathbf{X}(q,t)) \cdot \mathbf{w}(\mathbf{x}) \right) \, d\mathbf{x} \, dq \\
&= \int_0^L \mathbf{F}(q,t) \langle \boldsymbol{\delta}_{\mathbf{X}(q,t)}, \mathbf{w} \rangle_{\boldsymbol{\mathcal{D}}',\boldsymbol{\mathcal{D}}} \, dq \\
&= \int_0^L \mathbf{F}(q,t) \mathbf{w}(\mathbf{X}(q,t)) dq.
\end{aligned} \tag{2.11}$$

We note that the integrand on the right-hand side in (2.11) is well defined for all functions $\mathbf{w}$ such that the trace $\mathbf{w}(\mathbf{X}(\cdot,t))$ along ∂B_t belongs to $\mathbf{L}^2((0,L))$. Since by assumption $\mathbf{X}(\cdot,t) : [0,L] \to \Omega, t \in (0,T)$, is a Lipschitz curve in Ω, the trace mapping

$$\begin{aligned} \tau_{\mathbf{x}} : \mathbf{V} &\to \mathbf{H}^{1/2}(\partial B_t) \\ \mathbf{w} &\to \mathbf{w}(\mathbf{X}(\cdot,t)) \end{aligned}$$

is well defined. Since $\boldsymbol{\mathcal{D}}(\Omega)$ is dense in $\mathbf{V}$, $\mathbf{f}(t)$ can be extended to a bounded linear functional on $\mathbf{V}$ which proves (2.8). □

Setting $\mathbf{H}^3_{per}((0,L)) := \{\mathbf{Y} \in \mathbf{H}^3((0,L)) \mid d^k\mathbf{Y}/dq^k(0) = d^k\mathbf{Y}/dq^k(L), 0 \le k \le 2\}$, the variational formulation of the immersed boundary system (2.7) reads as follows: Given an initial velocity $\mathbf{v}_0 \in \mathbf{L}^2(\Omega)$, an initial configuration $\mathbf{X}_0 \in \mathbf{H}^3_{per}((0,L))$, and a force density $\mathbf{F}$, find the velocity field $\mathbf{v} \in \mathbf{H}^1((0,T),\mathbf{V}^*) \cap \mathbf{L}^2((0,T),\mathbf{V})$, $\mathbf{V} := \mathbf{H}^1_{0,\partial\Omega_D}$, the pressure $p \in L^2((0,T),L^2(\Omega))$, and $\mathbf{X} \in \mathbf{H}^1((0,T),\mathbf{Z}^*) \cap \mathbf{L}^2((0,T),\mathbf{Z})$, $\mathbf{Z} := \mathbf{H}^3_{per}((0,L))$, such that for all $\mathbf{w} \in \mathbf{V}$ and $q \in L^2(\Omega)$ it holds

$$\langle \rho_f \frac{\partial \mathbf{v}}{\partial t}, \mathbf{w}\rangle_{\mathbf{V}^*,\mathbf{V}} + a(\mathbf{v},\mathbf{w}) - b(p,\mathbf{w}) = \ell(\mathbf{w}) \quad \text{f.a.a. } t \in (0,T), \tag{2.12a}$$

$$b(q,\mathbf{v}(\cdot,t)) = 0 \quad \text{f.a.a. } t \in (0,T), \tag{2.12b}$$

$$\mathbf{v}(\cdot,0) = \mathbf{v}_0, \tag{2.12c}$$

$$\frac{\partial \mathbf{X}}{\partial t} = \mathbf{v}(\mathbf{X}(\cdot,t),t) \quad \text{f.a.a. } t \in (0,T), \tag{2.12d}$$

$$\mathbf{X}(\cdot,0) = \mathbf{X}_0. \tag{2.12e}$$

Here, $a(\cdot,\cdot)$, $b(\cdot,\cdot)$ and the linear functional $\ell(\cdot)$ are given by

$$a(\mathbf{v},\mathbf{w}) := (\rho_f(\mathbf{v}\cdot\nabla)\mathbf{v},\mathbf{w})_{0,\Omega} + (\eta\nabla\mathbf{v},\nabla\mathbf{w})_{0,\Omega} \tag{2.13a}$$

$$b(q,\mathbf{v}) := (q,\nabla\cdot\mathbf{v})_{0,\Omega} \tag{2.13b}$$

$$\ell(\mathbf{w}) := \langle\mathbf{f},\mathbf{w}\rangle_{\mathbf{V}^*,\mathbf{V}} = \int_0^L \mathbf{F}(\bar{q},t)\cdot\mathbf{w}(\mathbf{X}(\bar{q},t))d\bar{q}. \tag{2.13c}$$

Remark 2.3.2. For the special case where the weak formulation of the Navier-Stokes equations in (3.8) is replaced by the weak form of the Stokes equations, the existence of a solution of the coupled system (3.8) has been shown in one spatial dimension by Boffi/Gastaldi in [7] using a fixed point argument and a compactness result. The generalization to higher dimensions and to the Navier-Stokes equations is not straightforward, since the proof requires some regularity properties of the velocity that are not easy to obtain. As far as the existence of a weak solution of the Navier-Stokes equations and its regularity is concerned, we refer to [23, 33, 47].

CHAPTER 3

Surface Acoustic Wave-Actuated Cell Sorting

In this chapter, which follows the exposition in [21], we consider the mathematical modeling and numerical simulation of high throughput sorting of two different types of biological cells (type I and type II) by a biomedical micro-electro-mechanical system (BioMEMS) whose operating behavior relies on surface acoustic wave (SAW) manipulated fluid flow in a microchannel. The BioMEMS consists of a separation channel with three inflow channels for injection of the carrier fluid and the cells, two outflow channels for separation, and an interdigital transducer (IDT) close to the lateral wall of the separation channel for generation of the SAWs. The cells can be distinguished by fluorescence. The inflow velocities are tuned such that without

SAW actuation a cell of type I leaves the device through a designated outflow channel. However, if a cell of type II is detected, the IDT is switched on and the SAWs change the direction of the fluid flow such that the cell leaves the separation channel through the other outflow boundary.

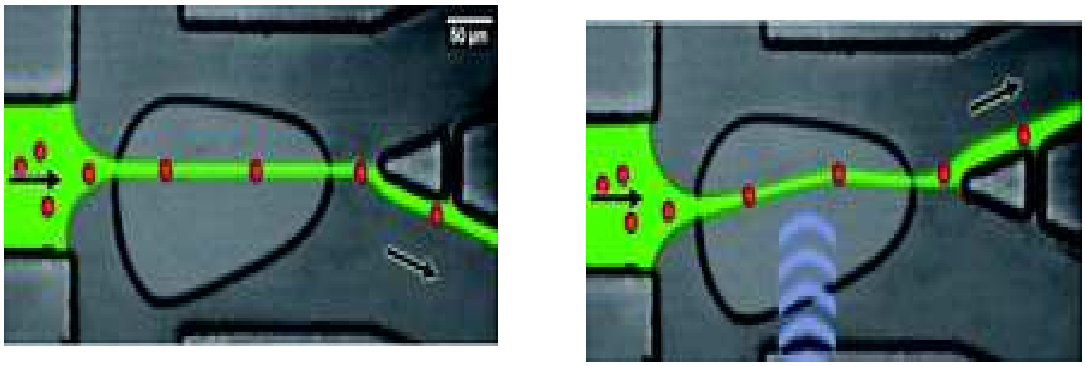

Figure 3.1: Surface acoustic wave actuated cell sorting (SAWACS) in a microfluidic PDMS channel (from [20]).

The motion of a cell in the carrier fluid is modeled by the Finite Element Immersed Boundary Method (FE-IB) described in the previous chapter. The generation of the SAWs is taken care of by the linearized equations of piezoelectricity, and the impact of the SAWs on the fluid flow is realized by means of a boundary condition for the Navier-Stokes equations. The discretization in space is done by P2/P1 Taylor-Hood elements for the fluid flow and periodic cubic splines for the immersed cell, whereas for discretization in time we use the backward Euler scheme for the Navier-Stokes equations and the forward Euler scheme for the equation of motion of the immersed cell. This Backward Euler/Forward Euler Finite Element Immersed Boundary Method (BE/FE FE-IB) requires a CFL-type condition for stability. Numerical results are presented that illustrate the feasibility of the surface acoustic

wave actuated cell sorting approach.

In section 3.1, we briefly discuss the linearized equations of piezoelectricity for SAW generation and the FE-IB method for modeling the fluid- cell interaction problem including stability estimates for the continuous as well as the fully discretized problem. In section 3.2 we present results of numerical simulation for the separation of a red blood cell (type I) and a melanoma breast cancer cell (type II).

3.1 Mathematical model

3.1.1 Surface acoustic wave (SAW) actuation

Surface acoustic waves are modes of elastic energy propagating at the surface of a solid body. They can be viewed as a nanometer-sized miniature of an earthquake. SAWs are easily excited on piezoelectric solids, because substrates deform due to the application of an electric field. Rapid changes of these electric fields are efficiently converted into a real nanoquake on a chip. Such rapid changes can be generated by a metallic electrode comb structure, called interdigital transducer (IDT). An IDT is used for the generation of the SAWs for the surface acoustic wave actuated cell sorting.

The separation channel is placed on top of a plastic chip partially coated by a piezoelectric substrate such as lithium niobate ($LiNbO_3$). The IDT is placed close to the wall of the channel with its aperture pointing towards the wall. A static electric field $\mathbf{E}$ is applied to generate a strain which varies across the aperture of the IDT.

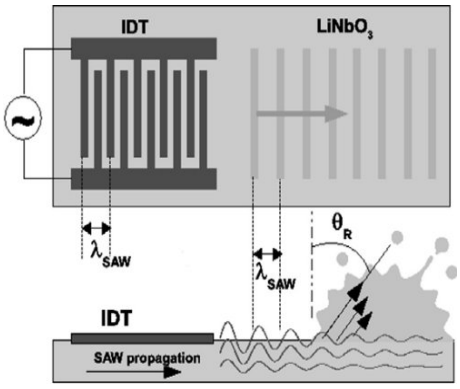

Figure 3.2: Interdigital Transducer (IDT) and motion of SAWs in the sagittal plane

In piezoelectric materials, the application of an electric field will cause a mechanical displacement of the material. They also show the reverse effect to generate an electric field when subjected to mechanical stress. These properties are called the piezoelectric effect and the inverse piezoelectric effect, respectively. In contrast to non-piezoelectric materials where the effect of stress tensor $\boldsymbol{\sigma}$ to the electric field $\mathbf{E}$ is quadratic, in piezoelectric materials $\boldsymbol{\sigma}$ depends linearly on $\mathbf{E}$ according to a generalized Hookes law:

$$\boldsymbol{\sigma}(\mathbf{u}, \mathbf{E}) = \mathbf{c}\varepsilon(\mathbf{u}) - \mathbf{e}\mathbf{E}, \tag{3.1}$$

Here, $\varepsilon(\mathbf{u}) := (\nabla\mathbf{u} + (\nabla\mathbf{u})^T)/2$ is the linearized strain tensor and $\mathbf{u}$ stands for the mechanical displacement, whereas $\mathbf{c}$ and $\mathbf{e}$ denote the symmetric fourth-order elasticity tensor and the symmetric third-order piezoelectric tensor, respectively. The origin of the piezoelectric effect is related to an asymmetry in the unit cell of a piezoelectric crystal and can be observed only in materials with a polar axis (cf.,

e.g., [24]).

Since the frequency of the electromagnetic wave is small compared to the frequency of the generated acoustic wave, a coupling will be neglected. Moreover, the electric field will be considered as quasistatic and irrotational. Hence, it can be expressed as the gradient of an electric potential Φ according to $\mathbf{E} = -\nabla\Phi$. Also, piezoelectric materials are nearly perfect insulators. Therefore , the only remaining quantity of interest in Maxwell's equations is the dielectric displacement $\mathbf{D}$ which is related to the electric field by the constitutive equation

$$\mathbf{D} = \boldsymbol{\epsilon}\mathbf{E} + \mathbf{P}, \tag{3.2}$$

where $\boldsymbol{\epsilon}$ is the electric permittivity of the material and $\mathbf{P}$ stands for the polarization. For piezoelectric materials, $\mathbf{P}$ depends linearly on the displacement $\mathbf{u}$ according to

$$\mathbf{P} = \mathbf{e}\varepsilon(\mathbf{u}). \tag{3.3}$$

We assume that the piezoelectric material with density $\rho_p > 0$ occupies some rectangular domain Ω_1 with boundary $\Gamma_1 = \partial\Omega_1$ and exterior unit normal $\mathbf{n}_1$. The boundary Γ_1 is partitioned into two disjoint sets in two ways according to

$$\Gamma_1 = \bar{\Gamma}_{E,D} \cup \bar{\Gamma}_{E,N}, \qquad \Gamma_{E,D} \cap \Gamma_{E,N} = \emptyset,$$
$$\Gamma_1 = \bar{\Gamma}_{p,D} \cup \bar{\Gamma}_{p,N}, \qquad \Gamma_{p,D} \cap \Gamma_{p,N} = \emptyset,$$

Given boundary data $\Phi_{E,D}$ on $\Gamma_{E,D}$, the pair $(\mathbf{u}, \Phi)$ satisfies the following initial-boundary value problem for the piezoelectric equations

$$\rho_p \frac{\partial^2 \mathbf{u}}{\partial t^2} - \nabla \cdot \boldsymbol{\sigma}(\mathbf{u}, \mathbf{E}) = 0 \qquad \text{in } \Omega_1 \times (0, T_1), \tag{3.4a}$$

$$\nabla \cdot \mathbf{D}(\mathbf{u}, \mathbf{E}) = 0 \qquad \text{in } \Omega_1 \times (0, T_1), \tag{3.4b}$$

$$\mathbf{u} = 0 \text{ on } \Gamma_{p,D}, \quad \mathbf{n}_1 \cdot \boldsymbol{\sigma} = \boldsymbol{\sigma}_{\mathbf{n}_1} \qquad \text{on } \Gamma_{p,N}, \tag{3.4c}$$

$$\Phi = \Phi_{E,D} \text{ on } \Gamma_{E,D}, \ \mathbf{n}_1 \cdot \mathbf{D} = \mathbf{D}_{\mathbf{n}_1} \qquad \text{on } \Gamma_{E,N}, \tag{3.4d}$$

$$\mathbf{u}(\cdot, 0) = \mathbf{0}, \quad \frac{\partial \mathbf{u}}{\partial t}(\cdot, 0) = \mathbf{0} \qquad \text{in } \Omega_1, \tag{3.4e}$$

together with the constitutive equations (3.1), (3.2) and (3.3).

Assuming time periodic excitations $\Phi_{E,D}(\cdot, t) = \mathrm{Re}\big(\hat{\Phi}_{E,D} \exp(-i\omega t)\big)$ such that $\hat{\Phi}_{E,D} \in H^{1/2}(\Gamma_{E,D})$, the time harmonic solutions are given in the form

$$\mathbf{u}(\cdot, t) = \mathrm{Re}(\mathbf{u}(\cdot) \exp(-i\omega t)), \ \Phi(\cdot, t) = \mathrm{Re}(\Phi(\cdot) \exp(-i\omega t)).$$

Further details can be found in [24].

3.1.2 The finite element immersed boundary method for fluid-cell interaction

Red blood cells (RBCs) and malignant cancer cells (MCF -7) are viscoelastic bodies consisting of a cytoskeleton enclosing a heterogeneous cell interior [1]. In a simplified biomechanical model, neglecting viscoelastic properties, the cytoskeleton can be represented as an elastic membrane with specific elastic moduli and the cell interior as an incompressible fluid with specific density and viscosity. We further assume that

the density and viscosity are the same as for the carrier fluid. In practice, this can be achieved via density and viscosity matching by adding chemicals to the carrier fluid. We note, however, that there exists a version of the FE-IB that can handle different densities and viscosities (cf., e.g., [6]). As we have already mentioned, the FE-IB method depends on three equations, namely, the incompressible Navier-Stokes equations, the material elasticity equations, and the interaction equations.

3.1.2.1 The incompressible Navier-Stokes equations

We consider a microchannel with a rectangular cross section, $\Omega \subset \mathbb{R}^2$, three inflow boundaries $\Gamma_{\text{in}}^{(i)} \subset \Gamma := \partial\Omega,\ i = 1 \leq i \leq 3$, two outflow boundaries $\Gamma_{\text{out}}^{(j)},\ j = 1, 2$ and a boundary Γ_{ac} where the SAWs enter the channel. We set $\Gamma_D := \partial\Omega \setminus \left(\bigcup_{i=1}^{3} \bar{\Gamma}_{\text{in}}^{(i)} \cup \bigcup_{j=1}^{2} \bar{\Gamma}_{\text{out}}^{(j)} \cup \bar{\Gamma}_{\text{ac}} \right)$ and $\Gamma' := \bigcup_{i=1}^{3} \bar{\Gamma}_{\text{in}}^{(i)} \cup \Gamma_{\text{ac}} \cup \Gamma_{\text{D}}$. (cf. Figure 3.3). For $T > 0$, we set $Q := \Omega \times (0, T],\ \Sigma_{\text{in}}^{(i)} := \Gamma_{\text{in}}^{(i)} \times (0, T],\ 1 \leq i \leq 3,\ \Sigma_{\text{out}}^{(j)} := \Gamma_{\text{out}}^{(j)} \times (0, T],\ 1 \leq j \leq 2,\ \Sigma_{\text{ac}} := \Gamma_{\text{ac}} \times (0, T]$, and $\Sigma_D := \Gamma_D \times (0, T]$.

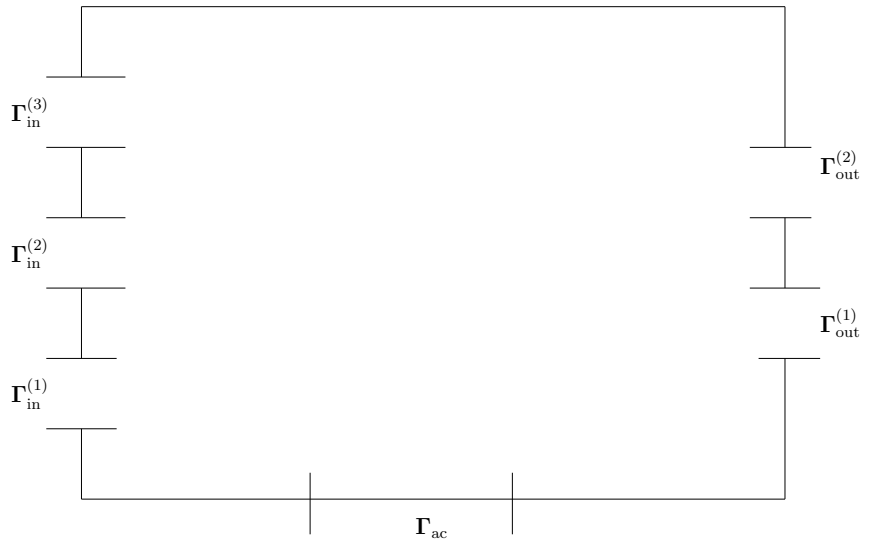

Figure 3.3: Separation channel

The incompressible Navier- Stokes equations that describe the fluid motion read:

$$\rho_f \left(\frac{\partial \mathbf{v}}{\partial t} + (\mathbf{v} \cdot \nabla)\mathbf{v} \right) - \nabla \cdot \boldsymbol{\sigma} = \mathbf{f} \qquad \text{in } Q, \tag{3.5a}$$

$$\nabla \cdot \mathbf{v} = 0 \qquad \text{in } Q, \tag{3.5b}$$

$$\mathbf{v} = \mathbf{v}_{\text{in}}^{(i)} \quad \text{on } \Sigma_{\text{in}}^{(i)},\ 1 \leq i \leq 3, \tag{3.5c}$$

$$\boldsymbol{\sigma}(\mathbf{v}, p)\mathbf{n} = \mathbf{0} \qquad \text{on } \Sigma_{\text{out}}^{(j)},\ j = 1, 2 \tag{3.5d}$$

$$\mathbf{v} = \mathbf{v}_{\text{ac}} \quad \text{on } \Sigma_{\text{ac}}, \tag{3.5e}$$

$$\mathbf{v} = \mathbf{0} \qquad \text{on } \Sigma_D, \tag{3.5f}$$

$$\mathbf{v} = \mathbf{v}^{(0)} \quad \text{in } \Omega, \tag{3.5g}$$

where $\mathbf{v}$ and p are the velocity field and the pressure, ρ_f is the density of the fluid, $\boldsymbol{\sigma}(\mathbf{v}, p) = 2\eta \mathbf{D}(\mathbf{v}) - pI$ is the stress tensor, where η is the dynamic viscosity of the

carrier fluid and $\mathbf{D}(\mathbf{v}) = (\nabla\mathbf{v} + (\nabla\mathbf{v})^T)/2$ stands for the rate of deformation tensor. Furthermore, $\mathbf{f}$ denotes the density of the body force exerted by the cell, $\mathbf{v}_{\text{ac}} = \mathbf{0}$ when the SAWs are not actuated and $\frac{\partial \mathbf{u}}{\partial t}$ when the IDT is switched on for SAW actuation. Here, $\mathbf{u}$ represents the mechanical displacement vector due to SAW. If the harmonically excited IDT is placed close to the lateral wall of the microchannel and we restrict ourselves to a two-dimensional scenario, we may assume $\mathbf{u} = (u_1, u_2)$ with

$$u_1 = 0, \qquad u_2 = a\sin(2\pi f t) \text{ on } \Sigma_{\text{ac}}, \tag{3.6}$$

where a is the amplitude and f stands for the operating frequency of the IDT. This leads to $\mathbf{v}_{\text{ac}} = (v_{\text{ac},1}, v_{\text{ac},1})^T$ with

$$v_{\text{ac},1} = 0, \qquad v_{\text{ac},2} = \frac{\partial u_2}{\partial t} = 2a\pi f\cos(2\pi f t) \text{ on } \Sigma_{\text{ac}}. \tag{3.7}$$

Introducing the function spaces

$$\begin{aligned}
\mathbf{V}(0,T) &:= \mathbf{H}^1((0,T), H^{-1}(\Omega)) \cap \mathbf{L}^2((0,T), \mathbf{H}^1(\Omega)),\\
\mathbf{W}(0,T) &:= \{\mathbf{v} \in \mathbf{V}(0,T) |\ \mathbf{v}|_{\Sigma_{\text{in}}^{(i)}} = \mathbf{v}_{\text{in}}^{(i)},\ 1 \le i \le 3,\ \mathbf{v}_{\Sigma_{\text{ac}}} = \mathbf{v}_{\text{ac}},\ \mathbf{v}_{\Sigma_D} = \mathbf{0}\}\\
Q(0,T) &:= L^2((0,T), L^2(\Omega)),
\end{aligned}$$

the weak formulation of the Navier-Stokes equations is to compute $(\mathbf{v}, p) \in \mathbf{W}(0,T) \times Q(0,T)$ such that for all $\mathbf{w} \in H^1_{0,\Gamma'}(\Omega)$ and all $q \in L^2(\Omega)$ there holds

$$\langle \rho_f \frac{\partial \mathbf{v}}{\partial t}, \mathbf{w}\rangle_{\mathbf{H}^{-1},\mathbf{H}^1_{0,\Gamma'}} + a(\mathbf{v},\mathbf{w}) - b(p,\mathbf{w}) = \langle \mathbf{f}, \mathbf{w}\rangle_{\mathbf{H}^{-1},\mathbf{H}^1_{0,\Gamma'}}, \tag{3.8a}$$

$$b(q,\mathbf{v}) = 0, \tag{3.8b}$$

$$\mathbf{v}(\cdot,0) = \mathbf{v}^{(0)}, \tag{3.8c}$$

where $a(\cdot,\cdot)$ and $b(\cdot,\cdot)$ are defined according to (2.13a) and (2.13b) .

3.1.2.2 Elasticity and interaction equations

We consider an immersed cell occupying a subdomain $B_t \subset \Omega,\ t \in [0,T]$, with boundary ∂B_t . As before, we assume that the curve ∂B_t is non self-intersecting and closed. We denote by $L := |\partial B_0|$ the length of the initial configuration ∂B_0 and by $\bar{q} \in [0,L]$, the Lagrangian coordinate labeling a material point on ∂B_0. $\mathbf{X}(\bar{q},t) = (\mathbf{X}_2(\bar{q},t), \mathbf{X}_2(\bar{q},t))^T$ will be the position at time $t \in (0,T]$ such that

$$\mathbf{X} \in \mathbf{H}^1((0,T), \mathbf{L}^2([0,L])) \cap \mathbf{L}^2((0,T), \mathbf{H}^3_{\text{per}}([0,L])), \tag{3.9}$$

where

$$\mathbf{H}^3_{\text{per}}([0,L]) := \{\mathbf{Y} \in \mathbf{H}^3([0,L]) \mid \partial^k \mathbf{Y}(0)/\partial \bar{q}^k = \partial^k \mathbf{Y}(L)/\partial \bar{q}^k,\ k = 0,1,2\}.$$

Let $\varepsilon_e(\mathbf{X}(\bar{q},t))$ and $\varepsilon_b(\mathbf{X}(\bar{q},t))$ such that

$$\varepsilon_e(\mathbf{X}(\bar{q},t)) = \frac{\kappa_e}{2}\left(\left|\frac{\partial \mathbf{X}}{\partial \bar{q}}\right|^2 - 1\right) \tag{3.10a}$$

$$\varepsilon_b(\mathbf{X}(\bar{q},t)) = \frac{\kappa_b}{2}\left|\frac{\partial^2 \mathbf{X}}{\partial \bar{q}^2}\right|^2 \tag{3.10b}$$

be the local energy densities on the elastic boundary ∂B_t where $\kappa_e > 0$ is the coefficient with respect to elongation-compression and $\kappa_b > 0$ is the elasticity coefficient with respect to bending. Then, the associated bending and elastic energies are given by

$$E_e(t) := \int_0^L \varepsilon_e(\mathbf{X}(\bar{q},t))d\bar{q}, \tag{3.11a}$$

$$E_b(t) := \int_0^L \varepsilon_b(\mathbf{X}(\bar{q},t))d\bar{q}, \tag{3.11b}$$

and the total energy reads:

$$E(t) := E_e(t) + E_b(t),\ t \in (0,T). \tag{3.12}$$

The local force density $\mathbf{F}$ is given in terms of the Gâteaux derivative of the total energy according to

$$\begin{aligned}\mathbf{F}(\bar{q},t) &= -E'(\mathbf{X}(\bar{q},t)) \\ &= \kappa_e \frac{\partial^2 \mathbf{X}}{\partial \bar{q}^2}(\bar{q},t) - \kappa_b \frac{\partial^4 \mathbf{X}}{\partial \bar{q}^4}(\bar{q},t).\end{aligned} \tag{3.13}$$

The global force density $\mathbf{f}$ in (3.5a) is given by

$$\langle \mathbf{f}(t), \mathbf{w} \rangle_{\mathbf{H}^{-1},\mathbf{H}^1_{0,\Gamma'}} = \int_0^L \mathbf{F}(\bar{q},t) \cdot \mathbf{w}(\mathbf{X}(\bar{q},t)) d\bar{q}, \qquad \mathbf{w} \in H^1_{0,\Gamma'}(\Omega) \tag{3.14}$$

Assuming additional regularity of $\mathbf{w}$, using (3.14) and integrating by parts, we get

$$\begin{aligned}\langle \mathbf{f}(t), \mathbf{w} \rangle_{\mathbf{H}^{-1},\mathbf{H}^1_{0,\Gamma'}} &= -\kappa_e \int_0^L \frac{\partial X(\cdot,t)}{\partial \bar{q}} \cdot \mathbf{D}\mathbf{w}(\mathbf{X}(\cdot,t)) \frac{\partial \mathbf{X}(\cdot,t)}{\partial \bar{q}} d\bar{q} \\ &\quad - \kappa_b \int_0^L \frac{\partial^2 \mathbf{X}(\cdot,t)}{\partial^2 \bar{q}^2} \cdot \mathbf{D}^2\mathbf{w}(\mathbf{X}(\cdot,t)) \cdot \left(\frac{\partial \mathbf{X}(\cdot,t)}{\partial \bar{q}}, \frac{\mathbf{X}(\cdot,t)}{\partial \bar{q}} \right) d\bar{q} \\ &\quad - \kappa_b \int_0^L \frac{\partial^2 \mathbf{X}(\cdot,t)}{\partial \bar{q}^2} \cdot \mathbf{D}\mathbf{w}(\mathbf{X}(\cdot,t)) \frac{\partial^2 \mathbf{X}(\cdot,t)}{\partial \bar{q}^2} d\bar{q}.\end{aligned} \tag{3.15}$$

In view of 3.15, the pointwise restriction of $\mathbf{w}$ and its first and second derivatives to ∂B_t have to be well-defined which requires $\mathbf{w}$ to be twice continuously differentiable on $\bar{B}_t$. This is guaranteed if we assume $\mathbf{w} \in \mathbf{H}^1_{0,\Gamma'}(\Omega) \cap \mathbf{H}^{3+\lambda}(\bar{B}_t),\ t \in [0,T]$, for some $\lambda \in (0,1/2)$, due to the Sobolev embedding theorem [46].

Moreover, the immersed cell moves with the velocity $\mathbf{v}$ of the carrier fluid and hence, we complement equations 3.8 with the equations of motion of the immersed boundary,

$$\frac{\partial \mathbf{X}}{\partial t}(\bar{q},t) = \mathbf{v}(\mathbf{X}(\bar{q},t),t), \quad (\bar{q},t) \in [0,L]\times(0,T], \tag{3.16a}$$

$$\mathbf{X}(\cdot,0) = \mathbf{X}^{(0)}(\cdot). \tag{3.16b}$$

In summary, we solve for $(\mathbf{v},p) \in \mathbf{W}(0,T)\times Q(0,T)$ and $\mathbf{X}$ as in (3.9) such that for all $\mathbf{w} \in \mathbf{H}^1_{0,\Gamma'}(\Omega)$ and $q \in Q(0,T)$, it holds

$$\langle \rho_f \frac{\partial \mathbf{v}}{\partial t}, \mathbf{w}\rangle_{\mathbf{H}^{-1},\mathbf{H}^1} + a(\mathbf{v},\mathbf{w}) - b(p,\mathbf{w}) = \langle \mathbf{f},\mathbf{w}\rangle_{\mathbf{H}^{-1},\mathbf{H}^1_{0,\Gamma'}}, \tag{3.17a}$$

$$b(q,\mathbf{v}) = 0, \tag{3.17b}$$

$$\mathbf{v}(\cdot,0) = \mathbf{v}^{(0)}, \tag{3.17c}$$

$$\frac{\partial \mathbf{X}}{\partial t}(\cdot,t) = \mathbf{v}(\mathbf{X}(\cdot,t),t), \tag{3.17d}$$

$$\mathbf{X}(\cdot,0) = \mathbf{X}^{(0)}(\cdot), \tag{3.17e}$$

where

$$\langle \mathbf{f}(t),\mathbf{w}\rangle_{\mathbf{H}^{-1},\mathbf{H}^1_{0,\Gamma'}} = \int_0^L \mathbf{F}(\bar{q},t)\cdot\mathbf{w}(\mathbf{X}(\bar{q},t))d\bar{q}.$$

3.1.3 Stability estimates

In case $\mathbf{v}|_\Sigma = \mathbf{0}$ and in the absence of a bending energy, a stability result has been established in [8]. A stability estimate for inflow and outflow boundary conditions of the form $\mathbf{n}_{\Gamma_{\text{in}}} \cdot \mathbf{v}|_{\Gamma_{\text{in}}} = -\mathbf{n}_{\Gamma_{\text{out}}} \cdot \mathbf{v}|_{\Gamma_{\text{out}}} = g$ with g being independent of $t \in [0,T]$ and in the presence of a bending energy has been provided in [22]. In the sequel, we will give a stability estimate under the boundary conditions as given by (3.5c)-(3.5f).

We suppose that the inflow velocities $\mathbf{v}_{\text{in}}^{(i)},\ 1 \le i \le 3$, and $\mathbf{v}_{\text{ac}}$ satisfy

$$\mathbf{v}_{\text{in}}^{(i)} \in \mathbf{H}^1((0,T), \mathbf{H}_{00}^{5/2+\lambda}(\Gamma_{\text{in}}^{(i)})),\ 1 \le i \le 3, \tag{3.18a}$$

$$\mathbf{v}_{\text{ac}} \in \mathbf{H}^1((0,T), \mathbf{H}_{00}^{5/2+\lambda}(\Gamma_{\text{ac}})), \tag{3.18b}$$

for some $\lambda \in (0, 1/2)$. We further construct $\mathbf{v}_{\text{out}}^{(j)},\ 1 \le j \le 2$, according to

$$\mathbf{v}_{\text{out}}^{(j)} \in \mathbf{H}^1((0,T), \mathbf{H}_{00}^{5/2+\lambda}(\Gamma_{\text{out}}^{(j)})),\ 1 \le j \le 2, \tag{3.19}$$

such that for $t \in [0,T]$ there holds

$$\begin{aligned} &\sum_{j=1}^{2} \int_{\Gamma_{\text{out}}^{(j)}} \mathbf{n}_{\Gamma_{\text{out}}} \cdot \mathbf{v}_{\text{out}}^{(j)}(s,t) ds + \sum_{i=1}^{3} \int_{\Gamma_{\text{in}}^{(i)}} \mathbf{n}_{\Gamma_{\text{in}}} \cdot \mathbf{v}_{\text{in}}^{(i)}(s,t) ds \\ &+ \int_{\Gamma_{\text{ac}}} \mathbf{n}_{\Gamma_{\text{ac}}} \cdot \mathbf{v}_{\text{ac}}(s,t) ds = 0. \end{aligned} \tag{3.20}$$

where $\mathbf{n}$ is the exterior unit normal for the respective boundaries.

Lemma 3.1.1. *If we assume (3.18a), (3.18b), (3.19), and (3.20), there exists a function*

$$\hat{\boldsymbol{\psi}} \in \mathbf{H}^1((0,T), \mathbf{H}^{3+\lambda}(\Omega) \cap \mathbf{H}(\text{div}^0, \Omega)), \tag{3.21}$$

such that

$$\hat{\boldsymbol{\psi}}(\cdot,t)|_{\Gamma_{\text{in}}^{(i)}} = \mathbf{v}_{\Gamma_{\text{in}}^{(i)}}(\cdot,t), \quad 1 \le i \le 3 \tag{3.22a}$$

$$\hat{\boldsymbol{\psi}}(\cdot,t)|_{\Gamma_{\text{out}}^{(j)}} = \mathbf{v}_{\Gamma_{\text{out}}^{(j)}}(\cdot,t), \quad 1 \le j \le 2 \tag{3.22b}$$

$$\hat{\boldsymbol{\psi}}(\cdot,t)|_{\Gamma_{\text{ac}}} = \mathbf{v}_{\Gamma_{\text{ac}}}(\cdot,t), \tag{3.22c}$$

Moreover, there exist constants $\hat{C}_1 > 0$ *and* $\hat{C}_2 > 0$ *such that for* $t \in [0,T]$ *it holds*

$$\|\hat{\boldsymbol{\psi}}(\cdot,t)\|_{\mathbf{C}^{2,\lambda}(\bar{\Omega})} \le \hat{C}_1 \; g_1(t), \tag{3.23a}$$

$$\int_0^t \|\frac{\partial \hat{\boldsymbol{\psi}}}{\partial \tau}(\cdot,\tau)\|^2_{\mathbf{C}^{2,\lambda}(\bar{\Omega})} \; d\tau \le \hat{C}_2 \; g_2(t), \tag{3.23b}$$

where the upper bounds $g_1(t)$ *and* $g_2(t)$ *are given by*

$$\begin{aligned} g_1(t) := & \sum_{i=1}^{3} \|\mathbf{v}_{\text{in}}^{(i)}(\cdot,t)\|_{\mathbf{H}_{00}^{5/2+\lambda}(\Gamma_{\text{in}}^{(i)})} + \sum_{j=1}^{2} \|\mathbf{v}_{\text{out}}^{(j)}(\cdot,t)\|_{\mathbf{H}_{00}^{5/2+\lambda}(\Gamma_{\text{out}}^{(i)})} \\ & + \|\mathbf{v}_{\text{ac}}(\cdot,t)\|_{\mathbf{H}_{00}^{5/2+\lambda}(\Gamma_{\text{ac}})}, \end{aligned} \tag{3.24a}$$

$$\begin{aligned} g_2(t) := & \int_0^t \Big(\sum_{i=1}^{3} \|\frac{\partial \mathbf{v}_{\text{in}}^{(i)}}{\partial \tau}(\cdot,\tau)\|^2_{\mathbf{H}_{00}^{5/2+\lambda}(\Gamma_{\text{in}}^{(i)})} + \sum_{j=1}^{2} \|\frac{\partial \mathbf{v}_{\text{out}}^{(j)}}{\partial \tau}(\cdot,\tau)\|^2_{\mathbf{H}_{00}^{5/2+\lambda}(\Gamma_{\text{out}}^{(i)})} \\ & + \|\frac{\partial \mathbf{v}_{\text{ac}}}{\partial \tau}(\cdot,\tau)\|^2_{\mathbf{H}_{00}^{5/2+\lambda}(\Gamma_{\text{ac}})} \Big) \; d\tau. \end{aligned} \tag{3.24b}$$

Proof. We denote by $\tilde{\mathbf{v}}_{\text{in}}^{(i)}(\cdot,t) \in \mathbf{H}^{5/2+\lambda}(\Gamma),\ 1 \le i \le 3,\ \tilde{\mathbf{v}}_{\text{out}}^{(j)}(\cdot,t) \in \mathbf{H}^{5/2+\lambda}(\Gamma),\ 1 \le j \le 2$, and $\tilde{\mathbf{v}}_{\text{ac}}(\cdot,t) \in \mathbf{H}^{5/2+\lambda}(\Gamma)$ the extensions of $\mathbf{v}_{\text{in}}^{(i)}(\cdot,t),\ \mathbf{v}_{\text{out}}^{(j)}(\cdot,t)$, and $\mathbf{v}_{\text{ac}}(\cdot,t)$ by zero to Γ such that

$$\|\tilde{\mathbf{v}}_{\mathrm{in}}^{(i)}(\cdot,t)\|_{5/2+\lambda,\Gamma} \lesssim \|\mathbf{v}_{\mathrm{in}}^{(i)}(\cdot,t)\|_{\mathbf{H}_{00}^{5/2+\lambda}(\Gamma_{\mathrm{in}}^{(i)})}, \tag{3.25a}$$

$$\|\tilde{\mathbf{v}}_{\mathrm{out}}^{(j)}(\cdot,t)\|_{5/2+\lambda,\Gamma} \lesssim \|\mathbf{v}_{\mathrm{out}}^{(j)}(\cdot,t)\|_{\mathbf{H}_{00}^{5/2+\lambda}(\Gamma_{\mathrm{out}}^{(i)})}, \tag{3.25b}$$

$$\|\tilde{\mathbf{v}}_{\mathrm{ac}}(\cdot,t)\|_{5/2+\lambda,\Gamma} \lesssim \|\mathbf{v}_{\mathrm{ac}}(\cdot,t)\|_{\mathbf{H}_{00}^{5/2+\lambda}(\Gamma_{\mathrm{ac}})}. \tag{3.25c}$$

In view of the trace theorem [46] there exist $\hat{\mathbf{v}}_{\mathrm{in}}^{(i)}(\cdot,t) \in \mathbf{H}^{3+\lambda}(\Omega), 1 \leq i \leq 3$, $\hat{\mathbf{v}}_{\mathrm{out}}^{(j)}(\cdot,t) \in \mathbf{H}^{3+\lambda}(\Omega), 1 \leq j \leq 2$, and $\hat{\mathbf{v}}_{\mathrm{ac}}(\cdot,t) \in \mathbf{H}^{3+\lambda}(\Omega)$ such that $\hat{\mathbf{v}}_{\mathrm{in}}^{(i)}|_{\Gamma}(\cdot,t) = \tilde{\mathbf{v}}_{\mathrm{in}}^{(i)}(\cdot,t)$, $\hat{\mathbf{v}}_{\mathrm{out}}^{(j)}|_{\Gamma}(\cdot,t) = \tilde{\mathbf{v}}_{\mathrm{out}}^{(j)}(\cdot,t)$ and $\hat{\mathbf{v}}_{\mathrm{ac}}|_{\Gamma}(\cdot,t) = \tilde{\mathbf{v}}_{\mathrm{ac}}(\cdot,t)$ as well as

$$\|\hat{\mathbf{v}}_{\mathrm{in}}^{(i)}(\cdot,t)\|_{3+\lambda,\Omega} \lesssim \|\tilde{\mathbf{v}}_{\mathrm{in}}^{(i)}(\cdot,t)\|_{5/2+\lambda,\Gamma}, \tag{3.26a}$$

$$\|\hat{\mathbf{v}}_{\mathrm{out}}^{(j)}(\cdot,t)\|_{3+\lambda,\Omega} \lesssim \|\tilde{\mathbf{v}}_{\mathrm{out}}^{(j)}(\cdot,t)\|_{5/2+\lambda,\Gamma}, \tag{3.26b}$$

$$\|\hat{\mathbf{v}}_{\mathrm{ac}}(\cdot,t)\|_{3+\lambda,\Omega} \lesssim \|\tilde{\mathbf{v}}_{\mathrm{ac}}(\cdot,t)\|_{5/2+\lambda,\Gamma}. \tag{3.26c}$$

Due to the Sobolev embedding theorem [46], $\mathbf{H}^{3+\lambda}(\Omega)$ is continuously embedded in $\mathbf{C}^{2,\lambda}(\bar{\Omega})$ and hence, there holds

$$\|\hat{\mathbf{v}}_{\mathrm{in}}^{(i)}(\cdot,t)\|_{\mathbf{C}^{2,\lambda}(\bar{\Omega})} \lesssim \|\hat{\mathbf{v}}_{\mathrm{in}}^{(i)}(\cdot,t)\|_{3+\lambda,\Omega}, \tag{3.27a}$$

$$\|\hat{\mathbf{v}}_{\mathrm{out}}^{(j)}(\cdot,t)\|_{\mathbf{C}^{2,\lambda}(\bar{\Omega})} \lesssim \|\hat{\mathbf{v}}_{\mathrm{out}}^{(j)}(\cdot,t)\|_{3+\lambda,\Omega}, \tag{3.27b}$$

$$\|\hat{\mathbf{v}}_{\mathrm{ac}}(\cdot,t)\|_{\mathbf{C}^{2,\lambda}(\bar{\Omega})} \lesssim \|\hat{\mathbf{v}}_{\mathrm{ac}}(\cdot,t)\|_{3+\lambda,\Omega}. \tag{3.27c}$$

We define

$$\hat{\boldsymbol{\psi}} := \sum_{i=1}^{3} \hat{\mathbf{v}}_{\mathrm{in}}^{(i)} + \sum_{j=1}^{2} \hat{\mathbf{v}}_{\mathrm{out}}^{(j)} + \hat{\mathbf{v}}_{\mathrm{ac}}. \tag{3.28}$$

By construction $\hat{\boldsymbol{\psi}} \in \mathbf{H}^1((0,T),\mathbf{H}^{3+\lambda}(\Omega))$ satisfies (3.22a)-(3.22c). Moreover, (3.23a) and (3.23b) hold true due to (3.25a)-(3.25c), (3.26a)-(3.26c), and (3.27a)-(3.27c).

Finally, (3.20) implies

$$\int_{\Omega} \nabla \cdot \hat{\boldsymbol{\psi}}(\cdot,t)dx = \int_{\Gamma} \mathbf{n} \cdot \hat{\boldsymbol{\psi}}|_{\Gamma}\, ds = 0,$$

and hence, $\hat{\boldsymbol{\psi}}(\cdot,t) \in \mathbf{H}(\mathrm{div}^0,\Omega),\ t \in [0,T]$. □

For the proof of the subsequent energy estimate, we note that the computational domain $\Omega \subset \mathbb{R}^2$ is such that for $\mathbf{v} \in \mathbf{W}(0,T)$ the Poincaré-Friedrichs inequality

$$\|\mathbf{v}(\cdot,t)\|_{0,\Omega} \leq C_{\Omega}\Big(\|\nabla \mathbf{v}(\cdot,t)\|^2_{0,\Omega} + \|\mathbf{v}(\cdot,t)\|^2_{0,\Gamma}\Big)^{1/2}, \quad t \in [0,T], \tag{3.29}$$

holds true for some constant $C_{\Omega} > 0$.

Theorem 3.1.2. *Let us suppose that the data of the problem satisfy* (3.18a),(3.18b) *and that the additional assumption*

$$\max_{0\leq t\leq T} g_1(t) \leq \frac{\eta}{16\ \rho_f\ \hat{C}_1\ C^2_{\Omega}} \tag{3.30}$$

holds true, where $g_1(t), t \in [0,T]$, *is from* (3.24a) *and the positive constants* $\hat{C}_1, C_{\Omega}$ *are given by* (3.23a),(3.29). *Moreover, assume that the triple* $(\mathbf{v}, p, \mathbf{X})$ *satisfies* (3.8a)-(3.8c) *and* (3.16a),(3.16b). *Then, there exists a positive constant* C, *depending on*

$\rho_f, \eta, \kappa_e, \kappa_b, \hat{C}_i, 0 \leq i \leq 2$, and C_Ω such that there holds

$$\begin{aligned}
&\frac{\rho_f}{4}\ \|\mathbf{v}(\cdot,t)\|_{0,\Omega}^2 + \frac{\eta}{8}\int_0^t \|\nabla\mathbf{v}(\cdot,t)\|_{0,\Omega}^2\ d\tau + \frac{\kappa_e}{2}\left\|\frac{\partial\mathbf{X}(\cdot,t)}{\partial\bar{q}}\right\|_{0,[0,L]}^2 + \frac{\kappa_b}{2}\left\|\frac{\partial^2\mathbf{X}(\cdot,t)}{\partial\bar{q}^2}\right\|_{0,[0,L]}^2 \\
&\leq C\Big(g_1(0)^2 + g_1(t)^2 + \int_0^t (g_1(\tau)^2 + g_2(\tau)^2)\ d\tau + \max_{0\leq\tau\leq t} g_1(\tau)\ \int_0^t \|\mathbf{v}(\cdot,\tau)\|_{0,\Gamma}^2\ d\tau \\
&+ \|\mathbf{v}^{(0)}\|_{0,\Omega}^2 + \left\|\frac{\partial\mathbf{X}^{(0)}}{\partial\bar{q}}\right\|_{0,[0,L]}^2 + \left\|\frac{\partial^2\mathbf{X}^{(0)}}{\partial\bar{q}^2}\right\|_{0,[0,L]}^2 + \int_0^t \left\|\frac{\partial\mathbf{X}(\cdot,\tau)}{\partial\bar{q}}\right\|_{0,[0,L]}^2\ d\tau \\
&+ \int_0^t \left\|\frac{\partial^2\mathbf{X}(\cdot,\tau)}{\partial\bar{q}^2}\right\|_{0,[0,L]}^2\ d\tau\Big).
\end{aligned} \tag{3.31}$$

Proof. Due to Lemma 3.1.1, $\mathbf{w} := \mathbf{v} - \hat{\boldsymbol{\psi}}$ is an admissible test function in (3.8a). Integrating over $[0,t]$, it follows that

$$\int_0^t \langle \rho_f \frac{\partial\mathbf{v}}{\partial\tau}, \mathbf{v} - \hat{\boldsymbol{\psi}}\rangle\ d\tau + \int_0^t a(\mathbf{v}, \mathbf{v} - \hat{\boldsymbol{\psi}})\ d\tau = \int_0^t \langle \mathbf{f}(\tau), \mathbf{v} - \hat{\boldsymbol{\psi}}\rangle_{\mathbf{H}^{-1},\mathbf{H}_0^1}\ d\tau. \tag{3.32}$$

Using integration by parts, Young's inequality with $\varepsilon_1 > 0$, and the Poincaré-Friedrichs inequality (3.29), the first term on the left-hand side in (3.32) can be

bounded from below according to

$$\int_0^t \langle \rho_f \frac{\partial \mathbf{v}}{\partial \tau}, \mathbf{v} - \hat{\boldsymbol{\psi}} \rangle_{\mathbf{H}^{-1},\mathbf{H}^1_{0,\Gamma'}} \, d\tau = \frac{\rho_f}{2} \int_0^t \frac{\partial}{\partial \tau} \|\mathbf{v}(\tau)\|^2_{0,\Omega} \, d\tau - \rho_f(\mathbf{v}(\cdot,t), \hat{\boldsymbol{\psi}}(\cdot,t))_{0,\Omega} \quad (3.33)$$

$$+ \rho_f(\mathbf{v}(\cdot,0), \hat{\boldsymbol{\psi}}(\cdot,0))_{0,\Omega} + \rho_f \int_0^t (\mathbf{v}(\cdot,\tau), \frac{\partial \hat{\boldsymbol{\psi}}}{\partial \tau}(\cdot,\tau))_{0,\Omega} \, d\tau \geq \frac{\rho_f}{4} \|\mathbf{v}(\cdot,t)\|^2_{0,\Omega} - \frac{3\rho_f}{4} \|\mathbf{v}(\cdot,0)\|^2_{0,\Omega}$$

$$- \rho_f \Big(\|\hat{\boldsymbol{\psi}}(\cdot,t)\|^2_{0,\Omega} + \|\hat{\boldsymbol{\psi}}(\cdot,0)\|^2_{0,\Omega} \Big) - \varepsilon_1 \rho_f \int_0^t \|\mathbf{v}(\cdot,\tau)\|^2_{0,\Omega} \, d\tau - \frac{\rho_f}{4\varepsilon_1} \int_0^t \|\frac{\partial \hat{\boldsymbol{\psi}}}{\partial \tau}(\cdot,\tau)\|^2_{0,\Omega} \, d\tau$$

$$\geq \frac{\rho_f}{4} \|\mathbf{v}(\cdot,t)\|^2_{0,\Omega} - \frac{3\rho_f}{4} \|\mathbf{v}(\cdot,0)\|^2_{0,\Omega} - \rho_f \Big(\|\hat{\boldsymbol{\psi}}(\cdot,t)\|^2_{0,\Omega} + \|\hat{\boldsymbol{\psi}}(\cdot,0)\|^2_{0,\Omega} \Big)$$

$$- \varepsilon_1 \rho_f C^2_\Omega \Big(\int_0^t \|\nabla \mathbf{v}(\cdot,\tau)\|^2_{0,\Omega} \, d\tau + \int_0^t \|\mathbf{v}(\cdot,\tau)\|^2_{0,\Gamma} \, d\tau \Big) - \frac{\rho_f}{4\varepsilon_1} \int_0^t \|\frac{\partial \hat{\boldsymbol{\psi}}}{\partial \tau}(\cdot,\tau)\|^2_{0,\Omega} \, d\tau.$$

Observing $(\rho_f(\mathbf{v} \cdot \nabla)\mathbf{v}, \mathbf{v})_{0,\Omega} = 0$ and by means of the Cauchy-Schwarz inequality, Young's inequality, and the Poincaré-Friedrichs inequality (3.29), the second term on the left-hand side in (3.32) can be estimated from below according to

$$\int_0^t a(\mathbf{v}, \mathbf{v} - \hat{\boldsymbol{\psi}}) \, d\tau \;\geq \quad (3.34)$$

$$\eta \int_0^t \|\nabla \mathbf{v}(\cdot,\tau)\|^2_{0,\Omega} \, d\tau - \eta \int_0^t \|\nabla \mathbf{v}(\cdot,\tau)\|_{0,\Omega} \|\nabla \hat{\boldsymbol{\psi}}(\cdot,\tau)\|_{0,\Omega} \, d\tau \; -$$

$$\rho_f \int_0^t \sum_{i,j=1}^{2} \|\mathbf{v}_j(\cdot,\tau)\|_{0,\Omega} \, \|\frac{\partial \mathbf{v}_i}{\partial x_j}(\cdot,\tau)\|_{0,\Omega} \, \|\hat{\boldsymbol{\psi}}_i(\cdot,\tau)\|_{0,\Omega} \, d\tau \;\geq$$

$$\Big(\frac{\eta}{2} - \rho_f \sqrt{2} \hat{C}_1 C^2_\Omega \max_{0 \leq \tau \leq t} g_1(\tau) \Big) \int_0^t \|\nabla \mathbf{v}(\cdot,\tau)\|^2_{0,\Omega} \, d\tau \; -$$

$$\frac{\rho_f \sqrt{2}}{2} C^2_\Omega \max_{0 \leq \tau \leq t} g_1(\tau) \int_0^t \|\mathbf{v}(\cdot,\tau)\|^2_{0,\Gamma} \, d\tau - \frac{\eta}{2} \int_0^t g_1(\tau)^2 \, d\tau.$$

In view of (3.15) and (3.16a), for the right-hand side in (3.32) we find

$$\int_0^t \langle \mathbf{f}(\tau), \mathbf{v}\rangle_{\mathbf{H}^{-1},\mathbf{H}^1_{0,\Gamma'}}\, d\tau \;=\; \tag{3.35}$$

$$\int_0^t \Big(-\kappa_e \int_0^L \frac{\partial \mathbf{X}(\bar{q},\tau)}{\partial \bar{q}} \cdot \frac{\partial}{\partial \bar{q}} \mathbf{v}(\mathbf{X}(\bar{q},\tau))\, d\bar{q} - \kappa_b \int_0^L \frac{\partial^2 \mathbf{X}(\bar{q},\tau)}{\partial \bar{q}^2} \cdot \frac{\partial^2}{\partial \bar{q}^2}\, \mathbf{v}(\mathbf{X}(\bar{q},\tau))\, d\bar{q}\Big) d\tau \;=$$

$$\int_0^t \Big(-\kappa_e \int_0^L \frac{\partial \mathbf{X}(\bar{q},\tau)}{\partial \bar{q}} \cdot \frac{\partial}{\partial \tau}\Big(\frac{\partial \mathbf{X}(\bar{q},\tau)}{\partial \bar{q}}\Big)\, d\bar{q} - \kappa_b \int_0^L \frac{\partial^2 \mathbf{X}(\bar{q},\tau)}{\partial \bar{q}^2} \cdot \frac{\partial}{\partial \tau}\Big(\frac{\partial^2 \mathbf{X}(\bar{q},\tau)}{\partial q^2}\Big)\, d\bar{q}\Big) d\tau$$

$$= \; -\frac{\kappa_e}{2} \int_0^t \frac{\partial}{\partial \tau}\, \|\frac{\partial \mathbf{X}}{\partial \bar{q}}(\tau)\|^2_{0,[0,L]}\, d\tau - \frac{\kappa_b}{2} \int_0^t \frac{\partial}{\partial \tau}\, \|\frac{\partial^2 \mathbf{X}}{\partial \bar{q}^2}(\tau)\|^2_{0,[0,L]}\, d\tau \;=$$

$$\frac{\kappa_e}{2}\Big(\|\frac{\partial \mathbf{X}}{\partial \bar{q}}(0)\|^2_{0,[0,L]} - \|\frac{\partial \mathbf{X}}{\partial \bar{q}}(t)\|^2_{0,[0,L]}\Big) + \frac{\kappa_b}{2}\Big(\|\frac{\partial^2 \mathbf{X}}{\partial \bar{q}^2}(0)\|^2_{0,[0,L]} - \|\frac{\partial^2 \mathbf{X}}{\partial \bar{q}^2}(t)\|^2_{0,[0,L]}\Big).$$

Using (3.15) again, we get

$$\int_0^t \langle \mathbf{f}(\tau), \hat{\mathbf{g}}\rangle_{\mathbf{H}^{-1},\mathbf{H}^1_{0,\Gamma'}}\, d\tau \;=\; \tag{3.36}$$

$$\kappa_e \int_0^t \Big(\frac{\partial \mathbf{X}}{\partial \bar{q}}, \mathbf{D}^1 \hat{\mathbf{g}}(\mathbf{X}(\cdot,\tau)) \frac{\partial \mathbf{X}}{\partial \bar{q}}\Big)_{0,[0,L]}\, d\tau + \kappa_b \int_0^t \Big(\frac{\partial^2 \mathbf{X}}{\partial \bar{q}^2}, \mathbf{D}^1 \hat{\mathbf{g}}(\mathbf{X}(\cdot,\tau)) \frac{\partial^2 \mathbf{X}}{\partial \bar{q}^2}\Big)_{0,[0,L]}\, d\tau$$

$$+ \; \kappa_b \int_0^t \Big(\frac{\partial^2 \mathbf{X}}{\partial \bar{q}^2}, \mathbf{D}^2 \hat{\mathbf{g}}(\mathbf{X}(\cdot,\tau))(\frac{\partial \mathbf{X}}{\partial \bar{q}}, \frac{\partial \mathbf{X}}{\partial \bar{q}})\Big)_{0,[0,L]}\, d\tau.$$

The stability estimate (3.31) now follows by using (3.33) with $\varepsilon_1 := \mu/(4\rho_f C_\Omega^2)$ and (3.34)-(3.36) in (3.32). □

3.1.4 Discretization in space and time

For discretization in space and time of the variational formulation of the FE-IB equations, we use the Backward Euler/Forward Euler Finite Element Immersed Boundary

Method (BE/FE FE-IB) from [22] in the sense that we discretize the Navier- Stokes equations by the backward Euler method in time and by Taylor-Hood P2/P1 elements in space, and we discretize the equation of motion of the immersed cell by the forward Euler scheme in time and by periodic cubic splines in space. In this subsection, we also give stability estimates for the fully discrete (BE/FE FE-IB).

3.1.4.1 Discretization in space

Let $\mathcal{T}_h$ be a geometrically conforming simplicial triangulation of Ω that aligns with the partition of Γ. For $K \in \mathcal{T}_h(\Omega)$, we denote the area of K by $|K|$, the diameter of K by h_K, and we set $h := \max\{h_K | K \in \mathcal{T}_h(\Omega)\}$. We assume that $\mathcal{T}_h(\Omega)$ is quasi-uniform, i.e., there exist constants $0 < c_Q \leq C_Q$ that only depend on the local geometry of the triangulation such that

$$c_Q h \leq h_K \leq C_Q h, \ K \in \mathcal{T}_h(\Omega). \tag{3.37}$$

Now, let $\mathcal{P}_k(K)$ be the space of polynomials of degree less or equal to k on K. For the spatial discretization of the weak formulation (2.2a)-(2.2c) of the incompressible Navier-Stokes equations we use P2-P1 Taylor-Hood elements [25, 27], i.e., we define

$$\mathbf{V}_h := \{\mathbf{v}_h \in \mathbf{C}(\bar{\Omega}) |\ \mathbf{v}_h|_K \in \mathcal{P}_2(K)^2, \ K \in \mathcal{T}_h(\Omega)\},$$
$$Q_h := \{q_h \in \mathbf{C}(\bar{\Omega}) |\ q_h|_K \in \mathcal{P}_1(K), \ K \in \mathcal{T}_h(\Omega)\},$$

and set $\mathbf{V}_{h,0} := \mathbf{V}_h \cap \mathbf{C}_0(\bar{\Omega})$. The finite element spaces $\mathbf{V}_h$ and Q_h are spanned by the canonically specified nodal basis functions:

$$\mathcal{B} = \{\phi_i\}_{i=1}^{n_1} \subset \mathbf{V}_h \text{ and } \mathcal{B}(Q_h) = \{\varphi_i\}_{i=1}^{n_2} \subset Q_h.$$

where $n_1 = \dim \mathbf{V}_h$ and $n_2 = \dim Q_h$. In particular, the inverse estimate

$$\|\mathbf{v}_h\|_{0,\Omega} \leq C_{inv} h^{-1} \|\nabla \mathbf{v}_h\|_{0,\Omega}, \ v_h \in \mathbf{V}_h, \tag{3.38}$$

holds true with a positive constant C_{inv} which is independent of h.

The discretization of the immersed boundary is done with respect to a partition

$$\mathcal{T}_{\Delta\bar{q}} := \{0 =: \bar{q}_0 < \bar{q}_1 < \cdots < \bar{q}_M := L\}, \ M \in \mathbb{N},$$

of the interval $[0, L]$ into subintervals $I_\ell := \ [\bar{q}_{\ell-1}, \bar{q}_\ell], \ 1 \leq \ell \leq M$, of length $\Delta\bar{q}_\ell := \bar{q}_\ell - \bar{q}_{\ell-1}$ with $\Delta\bar{q} := \max\{\Delta\bar{q}_\ell |\ 1 \leq \ell \leq M\}$.

We approximate $\mathbf{X}$ in (3.9) by periodic cubic splines and define

$$\begin{aligned} \mathbf{S}_h := \{\mathbf{Y}_h \in \mathbf{C}^2([0, L]; \Omega) \mid \mathbf{Y}_h|_{I_\ell} \in P_3(I_\ell)^2, \ 1 \leq \ell \leq M, \\ \mathbf{Y}_h^{(k)}(\bar{q}_0) = \mathbf{Y}_h^{(k)}(\bar{q}_M), \ k = 0, 1, 2\}, \end{aligned}$$

where $P_3(I_\ell)$ is the set of polynomials of degree ≤ 3 on I_ℓ. For $\mathbf{Y}_h \in \mathbf{S}_h$, we set $\mathbf{Y}_\ell := \mathbf{Y}_h(\bar{q}_\ell), \ 0 \leq \ell \leq M$.

The discrete immersed cell occupies subdomains $B_{h,t} \subset \Omega$ with boundaries $\partial B_{h,t}$ that are C^2 curves described by the periodic cubic spline $\mathbf{X}_h(\cdot, t) \in \mathbf{S}_h$.

3.1.4.2 Discrete elastic and bending energy

The discrete elastic energy E_h^e due to elongation/compression and the discrete bending energy E_h^b are given by

$$E_h^e(t) = \kappa_e \int_0^L \left(|\frac{\partial \mathbf{X}_h}{\partial \bar{q}}(\bar{q},t)|^2 - 1 \right) d\bar{q}, \tag{3.39}$$

$$E_h^b(t) = \kappa_b \sum_{\ell=1}^{M} \int_{\bar{q}_{\ell-1}}^{\bar{q}_\ell} |\frac{\partial^2 \mathbf{X}_h}{\partial \bar{q}^2}(\bar{q},t)|^2 d\bar{q}, \tag{3.40}$$

resulting in the discrete total energy

$$E_h(t) := E_h^e(t) + E_h^e(t)$$

The discrete force exerted by the immersed body is given by means of

$$\begin{aligned}
\langle \mathbf{f}_h(t), \mathbf{w}_h \rangle &= \langle -E_h'(t), \mathbf{w}_h \rangle_h \\
&= -\kappa_e \int_0^L \frac{\partial \mathbf{X}_h}{\partial \bar{q}} \cdot \frac{\partial}{\partial \bar{q}} \mathbf{w}_h(\mathbf{X}_h(\bar{q},t)) d\bar{q} \\
&\quad + \kappa_b \sum_{\ell=1}^{M} \int_{\bar{q}_{\ell-1}}^{\bar{q}_\ell} \frac{\partial^3 \mathbf{X}_h}{\partial \bar{q}^3} \cdot \frac{\partial}{\partial \bar{q}} \mathbf{w}_h(\mathbf{X}_h(\bar{q},t)) d\bar{q}.
\end{aligned}$$

Observing that $\frac{\partial^3 \mathbf{X}_h}{\partial \bar{q}^3}(\bar{q},t)$ is constant in I_ℓ, we obtain

$$\begin{aligned}
\langle \mathbf{f}_h(t), \mathbf{w}_h \rangle = & -\kappa_e \int_0^L \frac{\partial \mathbf{X}_h}{\partial \bar{q}} \cdot \nabla \mathbf{w}_h(\mathbf{X}_h(\bar{q},t)) \frac{\partial \mathbf{X}_h}{\partial \bar{q}} d\bar{q} \\
& + \kappa_b \sum_{\ell=1}^{M} \frac{\partial^3 \mathbf{X}_h}{\partial \bar{q}^3}|_{I_\ell} \cdot \int_{\bar{q}_{\ell-1}}^{\bar{q}_\ell} \nabla \mathbf{w}_h(\mathbf{X}_h(\bar{q},t)) \frac{\partial \mathbf{X}_h}{\partial \bar{q}} d\bar{q}.
\end{aligned} \tag{3.41}$$

If we approximate $\partial B_{h,t}$ by a closed polygon with vertices $\mathbf{X}_\ell(t) = \mathbf{X}(\bar{q}_\ell, t),\ 1 \le \ell \le M$, the second derivatives $\frac{\partial^2 \mathbf{X}_\ell(t)}{\partial \bar{q}^2}$ by $D^2_{\Delta\bar{q}}\mathbf{X}_\ell(t)$ such that

$$D^2_{\Delta\bar{q}}\mathbf{X}_\ell(t) = \frac{\mathbf{X}_{\ell+1}(t) - 2\mathbf{X}_\ell(t) + \mathbf{X}_{\ell-1}(t)}{(\Delta\bar{q})^2},$$

and the integrals in (3.40) by the trapezoidal rule, we obtain an approximation of $E^b_h(t)$ according to

$$E^b_h(t) \approx \frac{\kappa_b}{2} \sum_{\ell=1}^{M} |D^2_{\Delta\bar{q}}\mathbf{X}_\ell(t)|^2 \Delta\bar{q}_\ell,$$

where the indexing of the boundary nodes are chosen in such a way that $\mathbf{X}_{\ell-1}$ and $\mathbf{X}_{\ell+1}$ are neighbors of $\mathbf{X}_\ell$, and $\mathbf{X}_{M+\ell} := \mathbf{X}_\ell,\ 1 \le \ell \le 2$, and $\mathbf{X}_{-1} := \mathbf{X}_{M-1}$. If we take $\Delta\bar{q}_\ell = \Delta\bar{q},\ 1 \le \ell \le M$, we get

$$|D^2_{\Delta\bar{q}}\mathbf{X}_i(t)|^2 = |(\mathbf{X}_{\ell+1} - \mathbf{X}_\ell)(t)||(\mathbf{X}_\ell - \mathbf{X}_{\ell-1})(t)| \cdot \frac{1}{(\Delta\bar{q})^4} \left(\frac{|(\mathbf{X}_{\ell+1} - \mathbf{X}_\ell)(t)|}{|(\mathbf{X}_\ell - \mathbf{X}_{\ell-1})(t)|} + \frac{|(\mathbf{X}_\ell - \mathbf{X}_{\ell-1})(t)|}{|(\mathbf{X}_{\ell+1} - \mathbf{X}_\ell)(t)|} - 2\cos(\alpha_\ell(t)) \right),$$

where $\alpha_\ell(t)$ is the angle between the vectors $(\mathbf{X}_{\ell+1} - \mathbf{X}_\ell)(t)$ and $(\mathbf{X}_\ell - \mathbf{X}_{\ell-1})(t)$. Assuming $|(\mathbf{X}_{\ell+1} - \mathbf{X}_\ell)(t)| \approx |(\mathbf{X}_\ell - \mathbf{X}_{\ell-1})(t)|$ and using the identity $\sin^2(\alpha_\ell(t)/2) = (1 - \cos(\alpha_\ell(t)))/2$, it follows that

$$|D^2_{\Delta\bar{q}}\mathbf{X}_i(t)|^2 \approx\ 4\frac{1}{(\Delta\bar{q})^4}|(\mathbf{X}_{\ell+1} - \mathbf{X}_\ell)(t)||(\mathbf{X}_\ell - \mathbf{X}_{\ell-1})(t)| \sin^2(\alpha_\ell(t)/2).$$

Then, introducing local bending rigidities

$$\kappa_b^{(\ell)} :=\ \frac{1}{(\Delta\bar{q})^2}\ \kappa_b|(\mathbf{X}_{\ell+1} - \mathbf{X}_\ell)(t)||(\mathbf{X}_\ell - \mathbf{X}_{\ell-1})(t)| \cos^2(\alpha_\ell(t)/2),$$

we obtain the frequently used approximation of the discrete bending energy cf. [48, 49].

$$E^b_h(t)\ \approx \frac{1}{2} \sum_{\ell=1}^{M} \kappa_b^{(\ell)} \left(\frac{\tan(\alpha_\ell(t)/2)}{2\Delta\bar{q}} \right)^2 \Delta\bar{q}. \tag{3.42}$$

3.1.5 Discretization in time

For the discretization in time we consider a uniform partition

$$\mathcal{T}_{\Delta t} := \ \{0 =: t_0 < t_1 < \cdots < t_N := T\},\ N \in \mathbb{N},$$

of the time interval $[0, T]$ into subintervals of length $\Delta t := T/N$. We use the backward Euler scheme for discretization of the Navier- Stokes equations of the fluid and the forward Euler method for the motion of the immersed structure.

Let $\mathbf{v}_h^{(n)}$ be an approximation of $\mathbf{v}_h \in \mathbf{V}_h$ at $t = t_n$ and denote by $\mathbf{X}_\ell^{(n)}$ the approximation of X_ℓ at $t = t_n$. We refer to $\mathbf{D}_{\Delta t}^+$ and $\mathbf{D}_{\Delta t}^-$ as the forward and backward difference operators, i.e,

$$\mathbf{D}_{\Delta t}^+ \mathbf{v}_h^{(n)} := (\mathbf{v}_h^{(n+1)} - \mathbf{v}_h^{(n)})/(\Delta t), \quad \mathbf{D}_{\Delta t}^- \mathbf{v}_h^{(n)} := (\mathbf{v}_h^{(n)} - \mathbf{v}_h^{(n-1)})/(\Delta t)$$

$$\mathbf{D}_{\Delta t}^+ \mathbf{X}_\ell^{(n)} := (\mathbf{X}_\ell^{(n+1)} - \mathbf{X}_\ell^{(n)})/(\Delta t), \quad \mathbf{D}_{\Delta t}^- \mathbf{X}_\ell^{(n)} := (\mathbf{X}_\ell^{(n)} - \mathbf{X}_\ell^{(n-1)})/(\Delta t).$$

For $t_n \in \mathcal{T}_{\Delta t}$, we define $\mathbf{v}_{\mathrm{h,in}}^{(i)}(\cdot, t_n), 1 \le i \le 2$, and $\mathbf{v}_{\mathrm{h,ac}}(\cdot, t_n)$ as the L^2-projections of $\mathbf{v}_{\mathrm{in}}^{(i)}(\cdot, t_n)$ onto $\mathbf{V}_h|_{\Gamma_{\mathrm{in}}^{(i)}}$ and of $\mathbf{v}_{\mathrm{ac}}(\cdot, t_n)$ onto $\mathbf{V}_h|_{\Gamma_{\mathrm{ac}}}$ respectively.
We set

$$\begin{aligned}\mathbf{W}_h^{(n)} := \{&\mathbf{w}_h^{(n)} \in \mathbf{C}(\bar{\Omega}) \mid \mathbf{w}_h^{(n)} \in \mathbf{V}_h,\ \mathbf{w}_h^{(n)}|_{\Gamma_{\mathrm{in}}^{(i)}} = \mathbf{v}_{\mathrm{h,in}}^{(i)}(\cdot, t_n),\\ &1 \le i \le 2,\ \mathbf{w}_h^{(n)}|_{\Gamma_{\mathrm{ac}}} = \mathbf{v}_{\mathrm{h,ac}}(\cdot, t_n),\ \mathbf{w}_h^{(n)}|_{\Gamma_D} = \mathbf{0}\},\\ Q_h^{(n)} := \{&q_h^{(n)} \in C(\bar{\Omega}) \mid q_h^{(n)}|_K \in Q_h\}.\end{aligned}$$

The BE/FE FE-IB reads as follows:

Given $\mathbf{v}_h^{(0)} \in \mathbf{W}_h^{(0)}$ and $\mathbf{X}_h^{(0)} \in \mathbf{S}_h$, for $n = 0, \ldots, M-1$ we perform the following two steps:

Step 1: Compute $(\mathbf{v}_h^{(n+1)}, p_h^{(n+1)}) \in \mathbf{W}_h^{(n+1)} \times Q_h^{(n+1)}$ such that for all $\mathbf{w}_h \in \mathbf{V}_{h,0}$

$$(\rho_f \mathbf{D}_{\Delta t}^{+} \mathbf{v}_h^{(n)}, \mathbf{w}_h)_{0,\Omega} + a(\mathbf{v}_h^{(n+1)}, \mathbf{w}_h) - b(p_h^{(n+1)}, \mathbf{w}_h) = \ell_h^{(n)}(\mathbf{w}_h), \tag{3.43a}$$

$$b(q_h, \mathbf{v}_h^{(n+1)}) = 0, \tag{3.43b}$$

$$\ell_h^{(n)}(\mathbf{w}_h) := \langle \mathbf{f}_h^{(n)}, \mathbf{w}_h \rangle, \tag{3.43c}$$

where

$$\begin{aligned} \langle \mathbf{f}_h^{(n)}(t), \mathbf{w}_h \rangle := & -\kappa_e \int_0^L \frac{\partial \mathbf{X}_h^{(n)}}{\partial \bar{q}} \cdot \nabla \mathbf{w}_h(\mathbf{X}_h^{(n)}(\bar{q}, t)) \frac{\partial \mathbf{X}_h^{(n)}}{\partial \bar{q}} d\bar{q} \\ & + \kappa_b \sum_{\ell=1}^{M} \frac{\partial^3 \mathbf{X}_h^{(n)}}{\partial \bar{q}^3}|_{I_\ell} \cdot \int_{\bar{q}_{\ell-1}}^{\bar{q}_\ell} \nabla \mathbf{w}_h(\mathbf{X}_h^{(n)}(\bar{q}, t)) \frac{\partial \mathbf{X}_h^{(n)}}{\partial \bar{q}} d\bar{q}. \end{aligned} \tag{3.44}$$

Step 2: Compute $\mathbf{X}_h^{(n+1)} \in \mathbf{S}_h$ according to

$$\mathbf{D}_{\Delta t}^{+} \mathbf{X}_\ell^{(n)} = \mathbf{v}_h^{(n+1)}(\mathbf{X}_\ell^{(n)}), \quad 1 \le \ell \le M. \tag{3.45}$$

3.1.6 Stability estimates for the fully discrete problem

To derive a stability estimate for the fully discrete problem, we note that the boundary $\partial B_{h,t_n}$ of the immersed cell at time t_n consists of C^2 segments $\partial B_{h,t_n}^{(\ell)}$ connecting the material points $\mathbf{X}_{h,\ell-1}^{(n)}$ and $\mathbf{X}_{h,\ell}^{(n)},\ 1 \le \ell \le M$.

Let

$$\mathcal{T}_h(\partial B_{h,t_n}^{(\ell)}) := \{K \in \mathcal{T}_h(\Omega) \mid K \cap \partial B_{h,t_n}^{(\ell)} \neq \emptyset\}.$$

Then, from (3.38), we have

$$\|\nabla \mathbf{v}_h^{(n+1)}\|_{0,\partial B_{h,t_n}^{(\ell)}}^2 \le \sum_{K \in \mathcal{T}_h(\partial B_{h,t_n}^{(\ell)})} C_K h_K^{-1} \|\nabla \mathbf{v}_h^{(n+1)}\|_{0,K}^2, \tag{3.46}$$

where C_K is a positive constant independent of h_K.

If we denote by $C_\ell^{(n)}$ the maximum number of C^2 curve segments contained in an element $K \in \mathcal{T}_h(\partial B_{h,t_n}^{(\ell)})$ and set

$$C_{\text{cell}} := c_Q^{-1} \max_{0 \le n \le N-1} \max_{1 \le \ell \le M} \Big(C_\ell^{(n)} \max_{K \in \mathcal{T}_h(\partial B_{h,t_n}^{(\ell)})} C_K \Big), \tag{3.47}$$

where c_Q is from (3.37), we obtain

$$\|\nabla \mathbf{v}_h^{(n+1)}\|_{0,\partial B_{h,tn}}^2 \le C_{\text{cell}} h^{-1} \|\nabla \mathbf{v}_h^{(n+1)}\|_{0,\Omega}^2. \tag{3.48}$$

Since $\partial \mathbf{X}_h^{(n)}/\partial \bar{q} \in \mathbf{C}^1([0,L]),\ 0 \le n \le N$, and considering the fact that the third derivatives $\partial^3 \mathbf{X}_h^{(n)}/\partial \bar{q}^3$ are constant vectors on $I_\ell,\ 1 \le \ell \le M$, we define

$$\Lambda_1 := \max_{0 \le n \le N} \max_{\bar{q} \in [0,L)} \left| \frac{\partial \mathbf{X}_h^{(n)}}{\partial \bar{q}} \right| \Delta \bar{q}, \quad \Lambda_2 := \max_{0 \le n \le N} \max_{1 \le \ell \le M} \left| \frac{\partial^3 \mathbf{X}_h^{(n)}}{\partial \bar{q}^3} |_{I_\ell} \right| \Delta \bar{q}. \tag{3.49}$$

Moreover, we refer to $\hat{\boldsymbol{\psi}}_h(\cdot, t_n)$ as the biquadratic spline interpoland of $\hat{\boldsymbol{\psi}}(\cdot, t_n)$ from Lemma 3.1.1. Then, there exist constants $C_2^{(k)} > 0$ such that

$$\|\mathbf{D}^k \hat{\boldsymbol{\psi}}_h(\cdot, t_n)\|_{\mathbf{C}^k(\bar{\Omega})} \leq C_2^{(k)} g_1^{(n)}, \ 0 \leq k \leq 2, \tag{3.50a}$$

$$\sum_{r=0}^{n-1} \|\mathbf{D}_{\Delta t}^{+} \hat{\boldsymbol{\psi}}_h(\cdot, t_r)\|_{\mathbf{C}^k(\bar{\Omega})} \leq C_2^{(k)} g_2^{(n)}, \ 0 \leq k \leq 2, \tag{3.50b}$$

where $g_1^{(n)} := g_1(t_n)$ with $g_1(t)$ from (3.24a), and $g_2^{(n)}$ is given by (cf. (3.24b))

$$g_2^{(n)} := \sum_{r=0}^{n-1} \Big(\sum_{i=1}^{3} \|\mathbf{D}_{\Delta t}^{+} \mathbf{v}_{\text{in}}^{(i)}(\cdot, t_r)\|^2_{\mathbf{H}_{00}^{5/2+\lambda}(\Gamma_{\text{in}}^{(i)})} + \sum_{i=1}^{2} \|\mathbf{D}_{\Delta t}^{+} \mathbf{v}_{\text{out}}^{(i)}(\cdot, t_r)\|^2_{\mathbf{H}_{00}^{5/2+\lambda}(\Gamma_{\text{out}}^{(i)})} + \|\mathbf{D}_{\Delta t}^{+} \mathbf{v}_{\text{ac}}(\cdot, t_r)\|^2_{\mathbf{H}_{00}^{5/2+\lambda}(\Gamma_{\text{ac}})} \Big) \ \Delta t.$$

Theorem 3.1.3. *Let* $(\mathbf{v}_h^{(n)}, p_h^{(n)}, \mathbf{X}_h^{(n)})_{n=0}^{N}$ *be the solution of the semi-implicit BE/FE FE-IB* (3.43a),(3.43b) *and* (3.45). *In addition to the assumptions* (3.18a),(3.18b) *let*

$$\max_{0 \leq n \leq N} g_1^{(n)} \leq \frac{\eta}{16 \ \rho_f \ C_2^{(1)} \ C_\Omega^2}. \tag{3.51}$$

be satisfied and suppose that the following CFL-condition holds true

$$\frac{\Delta t}{h} \leq \frac{\eta}{8 C_{cell}(\kappa_e \Lambda_1 + \kappa_b \Lambda_2)}, \tag{3.52}$$

where the positive constants $C_\Omega, C_{cell}, C_2^{(1)}$, *and* Λ_1, Λ_2 *are from* (3.29),(3.47),(3.50a), *and* (3.49). *Then, there exists a positive constant* C, *depending on* $\rho, \eta, \kappa_e, \kappa_b, C_2^{(k)}, 0 \leq$

$k \leq 2$, and $C_\Omega, C_{cell}, \Lambda_1, \Lambda_2$ such that the following stability estimate is fulfilled

$$\frac{\rho_f}{4}\ \|\mathbf{v}_h^{(n)}\|_{0,\Omega}^2 + \frac{\eta}{16}\sum_{r=0}^{n}\|\nabla\mathbf{v}_h^{(r)}\|_{0,\Omega}^2\ \Delta t + \frac{\kappa_e}{2}\left\|\frac{\partial\mathbf{X}_h^{(n)}}{\partial\bar{q}}\right\|_{0,[0,L]}^2 \tag{3.53}$$

$$+\ \frac{\kappa_b}{2}\left\|\frac{\partial^2\mathbf{X}_h^{(n)}}{\partial\bar{q}^2}\right\|_{0,[0,L]}^2 \leq\ C\Big((g_1^{(0)})^2 + (g_1^{(n)})^2 + \sum_{r=0}^{n-1}\Big((g_1^{(r)})^2 + (g_2^{(r)})^2\Big)\Delta t$$

$$+\ \max_{0\leq r\leq n-1} g_1^{(r)}\sum_{r=0}^{n}\|\mathbf{v}_h^{(r)}\|_{0,\Gamma}^2\Delta t + \|\mathbf{v}_h^{(0)}\|_{0,\Omega}^2 + \left\|\frac{\partial\mathbf{X}_h^{(0)}}{\partial\bar{q}}\right\|_{0,[0,L]}^2 + \left\|\frac{\partial^2\mathbf{X}_h^{(0)}}{\partial\bar{q}^2}\right\|_{0,[0,L]}^2$$

$$+\ \sum_{r=1}^{n-1}\left\|\frac{\partial\mathbf{X}_h^{(r)}}{\partial\bar{q}}\right\|_{0,[0,L]}^2\Delta t + \sum_{r=1}^{n-1}\left\|\frac{\partial^2\mathbf{X}_h^{(r)}}{\partial\bar{q}^2}\right\|_{0,[0,L]}^2\Delta t\Big).$$

Proof. We choose $\mathbf{w}_h = \mathbf{v}_h^{(r+1)} - \hat{\boldsymbol{\psi}}_h^{(r+1)}$ in (3.43a), multiply both sides of the equation by Δt and sum over r ($r = 0$ to $r = n-1,\ n \leq N$). We thus obtain

$$\sum_{r=0}^{n-1}\Big((\rho_f\mathbf{D}_{\Delta t}^{+}\mathbf{v}_h^{(r)}, \mathbf{v}_h^{(r+1)} - \hat{\boldsymbol{\psi}}_h^{(r+1)})_{0,\Omega} +\ a(\mathbf{v}_h^{(r+1)}, \mathbf{v}_h^{(r+1)} - \hat{\boldsymbol{\psi}}_h^{(r+1)})\Big)\Delta t \tag{3.54}$$

$$= \sum_{r=0}^{m-1}\langle\mathbf{F}_h^{(r)}, \mathbf{v}_h^{(r+1)} - \hat{\boldsymbol{\psi}}_h^{(r+1)}\rangle_h\Delta t.$$

By summation by parts we get

$$\sum_{r=0}^{n-1}(\mathbf{D}^{+}_{\Delta t}\mathbf{v}_h^{(r)},\mathbf{v}_h^{(r+1)})_{0,\Omega}\Delta t = \frac{1}{2}(\|\mathbf{v}_h^{(n)}\|^2_{0,\Omega}-\|\mathbf{v}_h^{(0)}\|^2_{0,\Omega}) + \frac{1}{2}\Delta t\sum_{r=0}^{n-1}\|\mathbf{D}^{+}_{\Delta t}\mathbf{v}_h^{(r)}\|^2_{0,\Omega}\Delta t, \tag{3.55a}$$

$$\sum_{r=0}^{n-1}(\mathbf{D}^{+}_{\Delta t}\mathbf{v}_h^{(r)},\hat{\boldsymbol{\psi}}_h^{(r+1)})_{0,\Omega}\Delta t = (\mathbf{v}_h^{(n)},\hat{\boldsymbol{\psi}}_h^{(n)})_{0,\Omega}-(\mathbf{v}_h^{(0)},\hat{\boldsymbol{\psi}}^{(0)})_{0,\Omega} - \sum_{r=0}^{n-1}(\mathbf{v}_h^{(r)},\mathbf{D}^{+}_{\Delta t}\hat{\boldsymbol{\psi}}_h^{(r)})_{0,\Omega}\Delta t. \tag{3.55b}$$

Then using Young's inequality with $\varepsilon_1 > 0$, and the Poincaré-Friedrichs inequality (3.29), the first term on the left-hand side in (3.54) can be bounded from below as follows

$$\begin{aligned}
&\sum_{r=0}^{n-1}(\rho_f\mathbf{D}^{+}_{\Delta t}\mathbf{v}_h^{(r)},\mathbf{v}_h^{(r+1)}-\hat{\boldsymbol{\psi}}_h^{(r+1)})_{0,\Omega}\Delta t \qquad (3.56)\\
&\geq \frac{\rho_f}{4}\ \|\mathbf{v}_h^{(n)}\|^2_{0,\Omega}-\rho_f\ \|\mathbf{v}_h^{(0)}\|^2_{0,\Omega}\ -\rho_f\ \|\hat{\boldsymbol{\psi}}_h^{(n)}\|^2_{0,\Omega}-\frac{\rho_f}{2}\ \|\hat{\boldsymbol{\psi}}_h^{(0)}\|^2_{0,\Omega}\\
&-\varepsilon_1\rho_f\sum_{r=0}^{n-1}\|\mathbf{v}_h^{(r)}\|^2_{0,\Omega}\Delta t-\frac{\rho_f}{4\varepsilon_1}\sum_{r=0}^{n-1}\|\mathbf{D}^{+}_{\Delta t}\hat{\boldsymbol{\psi}}_h^{(r)}\|^2_{0,\Omega}\Delta t\\
&\geq \frac{\rho_f}{4}\ \|\mathbf{v}_h^{(n)}\|^2_{0,\Omega}-\rho_f\ \|\mathbf{v}_h^{(0)}\|^2_{0,\Omega}-\rho_f\ \|\hat{\boldsymbol{\psi}}_h^{(n)}\|^2_{0,\Omega}-\frac{\rho_f}{2}\ \|\hat{\boldsymbol{\psi}}_h^{(0)}\|^2_{0,\Omega}\ -\\
&\varepsilon_1\rho_f C_\Omega^2\Big(\sum_{r=0}^{n-1}\|\nabla\mathbf{v}_h^{(r)}\|^2_{0,\Omega}\Delta t+\sum_{r=0}^{n-1}\|\mathbf{v}_h^{(r)}\|^2_{0,\Gamma}\Delta t\Big)-\frac{\rho_f}{4\varepsilon_1}\sum_{r=0}^{n-1}\|\mathbf{D}^{+}_{\Delta t}\hat{\boldsymbol{\psi}}_h^{(r)}\|^2_{0,\Omega}\Delta t.
\end{aligned}$$

For the second term on the left-hand side in (3.54), as in the proof of Theorem 3.1.2, we deduce the following lower bound.

$$\begin{aligned}
&\sum_{r=0}^{n-1} a(\mathbf{v}_h^{(r+1)}, \mathbf{v}_h^{(r+1)} - \hat{\boldsymbol{\psi}}_h^{(r+1)})\ \Delta t \qquad (3.57)\\
&\geq\ \eta \sum_{r=0}^{n-1} \|\nabla \mathbf{v}_h^{(r+1)}(\cdot,\tau)\|_{0,\Omega}^2\ \Delta t - \eta \sum_{r=0}^{n-1} \|\nabla \mathbf{v}_h^{(r+1)}\|_{0,\Omega} \|\nabla \hat{\boldsymbol{\psi}}_h^{(r+1)}\|_{0,\Omega}\ \Delta t\\
&- \rho_f \sum_{r=0}^{n-1} \sum_{i,j=1}^{2} \|\mathbf{v}_{h,j}^{(r+1)}\|_{0,\Omega}\ \|\frac{\partial \mathbf{v}_{h,i}^{(r+1)}}{\partial x_j}\|_{0,\Omega}\ \|\hat{\boldsymbol{\psi}}_{h,i}^{(r+1)}\|_{0,\Omega}\ d\tau\\
&\geq \Big(\frac{\eta}{2} - \rho_f \sqrt{2} C_\Omega^2\ \max_{1\leq r\leq n} g_1(t_r)\Big) \sum_{r=0}^{n-1} \|\nabla \mathbf{v}_h^{r+1)}\|_{0,\Omega}^2\ \Delta t\\
&- \frac{\rho_f \sqrt{2}}{2} C_\Omega^2 \max_{1\leq r\leq n} g_1(t_r) \sum_{r=0}^{n-1} \|\mathbf{v}_h^{(r+1)}\|_{0,\Gamma}^2\ \Delta t - \frac{\eta}{2} \sum_{r=0}^{n-1} g_1(t_r)^2\ \Delta t.
\end{aligned}$$

Observing (3.41) and (3.45), for the right-hand side in (3.54) we obtain

$$\begin{aligned}
&\sum_{r=0}^{n-1} \langle \mathbf{f}_h^{(r)}, \mathbf{v}_h^{(r+1)} - \hat{\boldsymbol{\psi}}_h^{(r+1)} \rangle_h \Delta t\ = \qquad (3.58)\\
&- \kappa_e \sum_{r=0}^{n-1} \int_0^L \frac{\partial \mathbf{X}_h^{(r)}}{\partial \bar{q}} \cdot \mathbf{D}_{\Delta t}^{+} \frac{\partial \mathbf{X}_h^{(r)}}{\partial \bar{q}}\ d\bar{q}\Delta t + \kappa_b \sum_{r=0}^{n-1} \sum_{\ell=1}^{M} \int_{\bar{q}_{\ell-1}}^{\bar{q}_\ell} \frac{\partial^3 \mathbf{X}_h^{(r)}}{\partial \bar{q}^3} \cdot \mathbf{D}_{\Delta t}^{+} \frac{\partial \mathbf{X}_h^{(r)}}{\partial \bar{q}}\ d\bar{q}\Delta t\\
&+ \kappa_e \sum_{r=0}^{n-1} \int_0^L \frac{\partial \mathbf{X}_h^{(r)}}{\partial \bar{q}} \cdot \mathbf{D}^1 \hat{\boldsymbol{\psi}}_h^{(r+1)} \frac{\partial \mathbf{X}_h^{(r)}}{\partial \bar{q}}\ d\bar{q}\Delta t + \kappa_b \sum_{r=0}^{n-1} \int_0^L \frac{\partial^2 \mathbf{X}_h^{(r)}}{\partial \bar{q}^2} \cdot \mathbf{D}^1 \hat{\boldsymbol{\psi}}_h^{(r+1)} \frac{\partial^2 \mathbf{X}_h^{(r)}}{\partial \bar{q}^2}\ d\bar{q}\Delta t\\
&+ \kappa_b \sum_{r=0}^{n-1} \int_0^L \frac{\partial^2 \mathbf{X}_h^{(r)}}{\partial \bar{q}^2} \cdot \mathbf{D}^2 \hat{\boldsymbol{\psi}}_h^{(r+1)} \Big(\frac{\partial \mathbf{X}_h^{(r)}}{\partial \bar{q}}, \frac{\partial \mathbf{X}_h^{(r)}}{\partial \bar{q}}\Big)\ d\bar{q}\Delta t.
\end{aligned}$$

Summation by parts yields

$$
\begin{aligned}
&-\kappa_e \sum_{r=0}^{n-1} \int_0^L \frac{\partial \mathbf{X}_h^{(r)}}{\partial \bar{q}} \cdot \mathbf{D}_{\Delta t}^{+} \frac{\partial \mathbf{X}_h^{(r)}}{\partial \bar{q}} \, d\bar{q}\Delta t \; = \qquad (3.59)\\
&+\kappa_e \sum_{r=0}^{n-1} \int_0^L \mathbf{D}_{\Delta t}^{+} \frac{\partial \mathbf{X}_h^{(r)}}{\partial \bar{q}} \cdot \frac{\partial \mathbf{X}_h^{(r+1)}}{\partial \bar{q}} \, d\bar{q}\Delta t + \kappa_e \Big(\int_0^L \left| \frac{\partial \mathbf{X}_h^{(0)}}{\partial \bar{q}} \right|^2 \, d\bar{q} - \int_0^L \left| \frac{\partial \mathbf{X}_h^{(n)}}{\partial \bar{q}} \right|^2 \, d\bar{q} \Big).
\end{aligned}
$$

For the first term on the right-hand side in (3.59) we have

$$
\begin{aligned}
&\kappa_e \sum_{r=0}^{n-1} \int_0^L \mathbf{D}_{\Delta t}^{+} \frac{\partial \mathbf{X}_h^{(r)}}{\partial \bar{q}} \cdot \frac{\partial \mathbf{X}_h^{(r+1)}}{\partial \bar{q}} \, d\bar{q}\Delta t = \qquad (3.60)\\
&\kappa_e \sum_{r=0}^{n-1} \int_0^L \frac{\partial \mathbf{X}_h^{(r)}}{\partial \bar{q}} \cdot \mathbf{D}_{\Delta t}^{+} \frac{\partial \mathbf{X}_h^{(r)}}{\partial \bar{q}} \, d\bar{q}\Delta t + \kappa_e \Delta t \sum_{r=0}^{n-1} \int_0^L \left| \mathbf{D}_{\Delta t}^{+} \frac{\partial \mathbf{X}_h^{(r)}}{\partial \bar{q}} \right|^2 \, d\bar{q}\Delta t.
\end{aligned}
$$

Using (3.45),(3.47), and (3.49) , for the last term on the right-hand side in (3.60) we get

$$
\begin{aligned}
\int_0^L \left| \mathbf{D}_{\Delta t}^{+} \frac{\partial \mathbf{X}_h^{(r)}}{\partial \bar{q}} \right|^2 \, d\bar{q} &= \int_0^L |\frac{\partial}{\partial \bar{q}} (\mathbf{v}_h^{(r+1)}(\mathbf{X}_h^{(r)}))|^2 \, d\bar{q} \qquad (3.61)\\
&\leq \int_0^L |\nabla \mathbf{v}_h^{(r+1)}(\mathbf{X}_h^{(r)})|^2 \left| \frac{\partial \mathbf{X}_h^{(r)}}{\partial \bar{q}} \right| \left| \frac{\partial \mathbf{X}_h^{(r)}}{\partial \bar{q}} \right| \, d\bar{q}\\
&\leq \Lambda_1 \|\nabla \mathbf{v}_h^{(r+1)}\|_{0,\partial B_{h,t_r}}^2 \leq C_{\text{cell}} \Lambda_1 h^{-1} \|\nabla \mathbf{v}_h^{(r+1)}\|_{0,\Omega}^2.
\end{aligned}
$$

Combining (3.59),(3.60) and (3.61) results in

$$
\begin{aligned}
&-\kappa_e \sum_{r=0}^{n-1} \int_0^L \frac{\partial \mathbf{X}_h^{(r)}}{\partial \bar{q}} \cdot \mathbf{D}_{\Delta t}^{+} \frac{\partial \mathbf{X}_h^{(r)}}{\partial \bar{q}} \, d\bar{q}\Delta t \; \leq \qquad (3.62)\\
&\frac{\kappa_e}{2} \Big(\left\| \frac{\partial \mathbf{X}_h^{(0)}}{\partial \bar{q}} \right\|_{[0,L]}^2 - \left\| \frac{\partial \mathbf{X}_h^{(n)}}{\partial \bar{q}} \right\|_{[0,L]}^2 \Big) + \frac{\kappa_e}{2} \, C_{\text{cell}} \Lambda_1 h^{-1} \Delta t \sum_{r=0}^{r-1} \|\nabla \mathbf{v}_h^{(r+1)}\|_{0,\Omega}^2 \Delta t.
\end{aligned}
$$

Similarly we obtain

$$\kappa_b \sum_{r=0}^{n-1} \sum_{\ell=1}^{M} \int_{\bar{q}_{\ell-1}}^{\bar{q}_\ell} \frac{\partial^3 \mathbf{X}_h^{(r)}}{\partial \bar{q}^3} \cdot \mathbf{D}_{\Delta t}^{+} \frac{\partial \mathbf{X}_h^{(r)}}{\partial \bar{q}} \, d\bar{q}\Delta t \; \leq \tag{3.63}$$

$$\frac{\kappa_b}{2} \Big(\left\| \frac{\partial^2 \mathbf{X}_h^{(0)}}{\partial \bar{q}^2} \right\|_{[0,L]}^2 - \left\| \frac{\partial^2 \mathbf{X}_h^{(n)}}{\partial \bar{q}^2} \right\|_{[0,L]}^2 \Big) + \frac{\kappa_b}{2} \, C_{\text{cell}} \Lambda_2 h^{-1} \Delta t \sum_{r=0}^{n-1} \|\nabla \mathbf{v}_h^{(r+1)}\|_{0,\Omega}^2 \Delta t.$$

Choosing $\varepsilon_1 := \eta/(4\rho_f C_\Omega^2)$ in (3.56), observing (3.51), using (3.52) in (3.62),(3.63), and estimating the remaining terms on the right-hand side in (3.58) from above as in the proof of Theorem 3.1.2 we conclude the result. □

3.2 Numerical simulations

In this section, we report on the results of numerical simulations for the separation of an RBC cell and melanoma cell in a channel using SAW manipulated fluid flow. Following [20], we consider a separation channel

$$\Omega = (0\mu m, 300\mu m) \times (0\mu m, 220\mu m)$$

with three inflow boundaries

$$\Gamma_{\text{in}}^{(1)} = \{0\} \times (30\mu m, 80\mu m),$$
$$\Gamma_{\text{in}}^{(2)} = \{0\} \times (90\mu m, 130\mu m),$$
$$\Gamma_{\text{in}}^{(3)} = \{0\} \times (150\mu m, 200\mu m),$$

two outflow boundaries

$$\Gamma_{\text{out}}^{(1)} = \{300\} \times (20\mu m, 100\mu m),$$
$$\Gamma_{\text{out}}^{(2)} = \{300\} \times (120\mu m, 200\mu m),$$

and a boundary

$$\Gamma_{\text{ac}} = (135\mu m, 165\mu m) \times \{0\},$$

where the SAWs enter the separation channel. The density ρ_f and the dynamic viscosity η have been chosen as

$$\rho_f = 1.0 \cdot 10^3 \text{kg/m}^3, \quad \eta = 6.0 \cdot 10^{-3} \text{Pa} \cdot \text{s}$$

both for the carrier fluid and the fluid enclosed by the membrane of the RBC and the melanoma cell. We have considered an RBC of diameter $7.5\mu m$, perimeter $P =$

19.8μm and moduli [44]

$$\kappa_e = 6.0 \cdot 10^{-6}\text{N/m}, \quad \kappa_b = 2.0 \cdot 10^{-19}\text{Nm},$$

a_0, a_1 and a_2 in (A.1) are taken to be $0.49, 1.17$ and -0.75 respectively. The reduced volume ratio $C_r = 0.587$.

The melanoma cell has been modeled as a sphere of diameter 16μm and moduli [3]

$$\kappa_e = 2.8 \cdot 10^{-6}\text{N/m}, \quad \kappa_b = 1.2 \cdot 10^{-19}\text{Nm}.$$

Scenario I: The first scenario represents an experimental set-up without SAW actuation (i.e., $\mathbf{v}_{\text{ac}} = \mathbf{0}$ on Σ_{ac}). An RBC enters the separation channel through the inlet $\Gamma_{\text{in}}^{(2)}$ and the inflow velocities $\mathbf{v}_{\text{in}}^{(i)}$ on $\Sigma_{\text{in}}^{(i)}, 1 \leq i \leq 3$, are chosen according to

$$\begin{aligned}
\mathbf{v}_{\text{in}}^{(1)} &= (v_{\text{in},1}^{(1)}, v_{\text{in},2}^{(1)})^T, \\
v_{\text{in},1}^{(1)} &= \hat{v}_{\text{in}}^{(1)} m_{\text{in}}^{(1)}(x_2)(x_2 - 30)(80 - x_2) \cos\alpha, \\
v_{\text{in},2}^{(1)} &= -\hat{v}_{\text{in}}^{(3)} m_{\text{in}}^{(1)}(x_2)(x_2 - 30)(80 - x_2) \sin\alpha, \\
\mathbf{v}_{\text{in}}^{(2)} &= (v_{\text{in},1}^{(2)}, v_{\text{in},2}^{(2)})^T, \\
v_{\text{in},1}^{(2)} &= \hat{v}_{\text{in}}^{(2)} m_{\text{in}}^{(2)}(x_2)(x_2 - 90)(130 - x_2), \\
v_{\text{in},2}^{(2)} &= 0, \\
\mathbf{v}_{\text{in}}^{(3)} &= (v_{\text{in},1}^{(3)}, v_{\text{in},2}^{(3)})^T, \\
v_{\text{in},1}^{(3)} &= \hat{v}_{\text{in}}^{(3)} m_{\text{in}}^{(3)}(x_2)(x_2 - 150)(200 - x_2) \cos\alpha, \\
v_{\text{in},2}^{(3)} &= -\hat{v}_{\text{in}}^{(3)} m_{\text{in}}^{(3)}(x_2)(x_2 - 150)(200 - x_2) \sin\alpha.
\end{aligned}$$

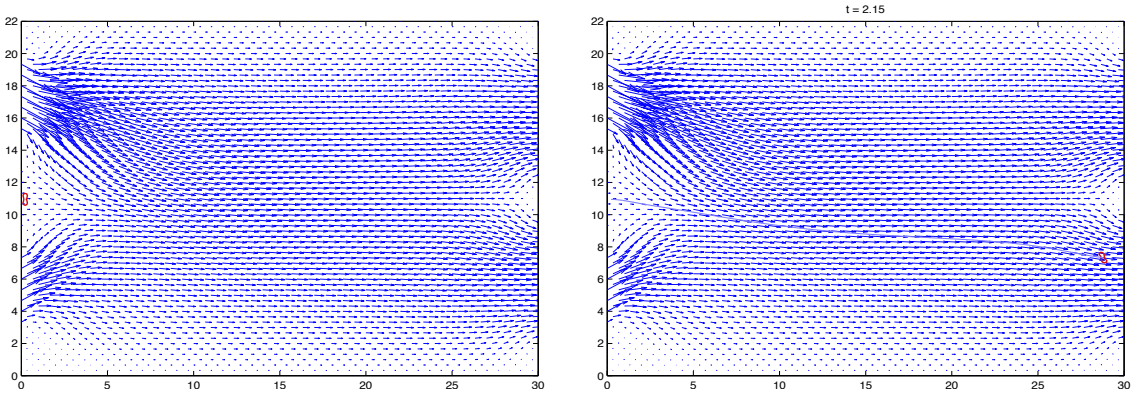

Figure 3.4: Velocity field and motion of an RBC without SAW actuation: Initial state after injection (left) and state shortly before the RBC leaves the separation channel (right)

Here , $b_1^{(1)} = 30, b_2^{(1)} = 80, b_1^{(2)} = 100, b_2^{(2)} = 130, b_1^{(3)} = 150, b_2^{(3)} = 200$, and $m_{\text{in}}^{(i)}(x_2), 1 \leq i \leq 3$, are smooth cut-off functions satisfying $m_{\text{in}}^{(i)}(x_2) = 1$ on $[b_1^{(i)} + \epsilon,\ b_1^{(i)} + \epsilon]$ and vanish at $b_1^{(i)}$ and $b_2^{(i)}$. The inflow velocities $\hat{v}_{\text{in}}^{(i)},\ 1 \leq i \leq 3$, and the angle α have been chosen by means of

$$\hat{v}_{\text{in}}^{(1)} = 5.0 \cdot 10^{-2} \text{ m/s}, \quad \hat{v}_{\text{in}}^{(1)} = 1.0 \cdot 10^{-2} \text{ m/s}, \quad \hat{v}_{\text{in}}^{(1)} = 10.0 \cdot 10^{-2} \text{ m/s}, \quad \alpha = \pi/6.$$

As can be seen in Figure A.1, the RBC leaves the separation channel through the outlet $\Gamma_{\text{out}}^{(1)}$.

We took mesh size $h = 1/3$ and time step $\Delta t = 1/400$. Dofs: 48146 (velocity), 6097 (pressure), 54243 (overall). We started at t_0=1/400 and stopped the simulation at final time $T = 2.5$, shortly after the RBC left the channel. The computation time for the semi implicit FE was 3 hours 51 minutes and 26 seconds.

Scenario II: The second scenario corresponds to a situation where a melanoma cell enters the separation channel though the inlet $\Gamma_{\text{in}}^{(2)}$, the inflow velocities are

chosen as in Scenario I, and SAWs are created by an IDT with operating frequency $f = 100.0$ MHz that enter the channel through Γ_{ac}. The impact of the SAWs on the fluid flow is realized by an inflow velocity $\mathbf{v}_{ac} = (v_{\text{ac, 1}}, v_{\text{ac, 1}})$ according to

$$v_{\text{ac, 1}} = 0.\ v_{\text{ac, 2}} = 2a\pi f m_{\text{ac}}(x_1)\cos(2\pi f t) \text{ on } \Sigma_{\text{ac}}.$$

Here, $a = 1.0 \cdot 10^{-9}$m and $m_{\text{ac}}(x_1)$ is smooth cut-off function satisfying$m_{\text{ac}}(x_1) = 1$ on $[a_1/2 - d_1 + \epsilon,\ a_1/2 + d_1 - \epsilon]$ and vanish at $b_1^{(i)}$.

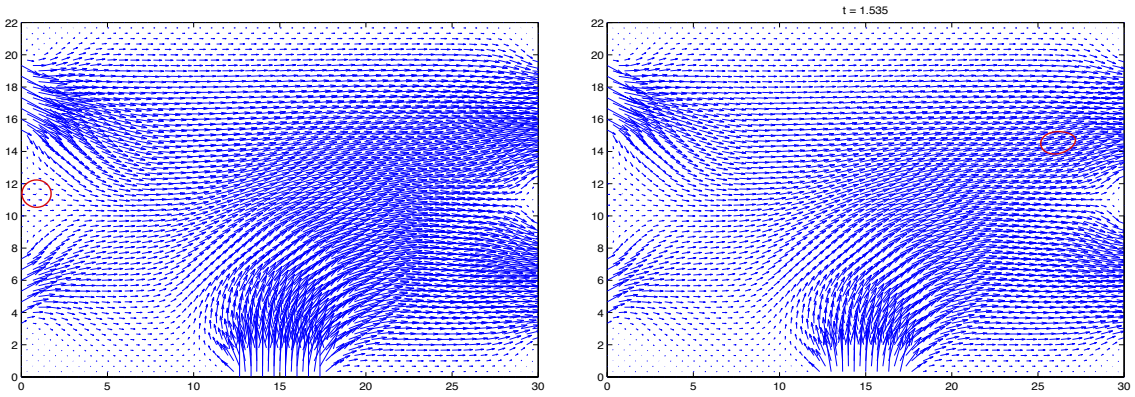

Figure 3.5: Velocity field and motion of a melanoma cell with SAW actuation: Initial state after injection (left) and state shortly before the cell leaves the separation channel (right)

Figure 3.5 displays the resulting velocity fields and the motion of the melanoma cell. Due to the SAW actuation, the path of the melanoma cell is diverted such that it leaves the separation channel through the outlet $\Gamma_{\text{out}}^{(2)}$.

The mesh size h is taken to be the same as in scenario I and $\Delta t = 1/40$. We started at $t_0 = 1/40$ and stopped the simulation at final time $T = 1.55$, shortly after the melanoma cell reaches the boundary. The computation time for the semi implicit FE in this case was 12 minutes. We notice that the time step is bigger than in the

case of scenario I. That is due to the CFL - condition, namely the dependence of the time step on the size of the immersed body.

All computations have been performed under Linux featuring Intel(R)Core(TM) i3-2100 CPU 3.10 GHz and 7.7 GB RAM.

CHAPTER 4

Surface Acoustic Wave-Actuated Enantiomer Separation

Chirality is formally defined as the geometric property of an object, e.g., a molecule, of not being superimposable with its mirror image. Molecules that can be superimposed on their mirror images are achiral (not chiral). It is a property found throughout biological systems, from the basic building blocks of life such as amino acids, carbohydrates, and lipids to the layout of the human body. Chirality is often illustrated with the idea of left- and right-handedness: a left hand and right hand are mirror images of each other but are not superimposable. The two mirror images of a chiral molecule are termed enantiomers (or optical isomers). Enantiomers typically occur as racemic compounds of left- and right-handed species which may

have completely different properties. Therefore, in applications such as drug design in pharmacology, enantiomer separation is an important issue.

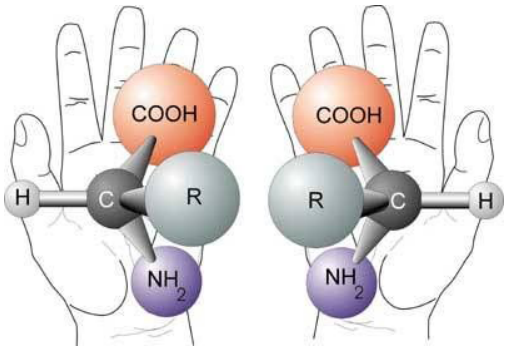

Figure 4.1: Left- and right-handed enantiomer

A famous example is the thalidomide tragedy in 1950s and 60s in Germany. Thalidomide was sold as the racemic mixture of enantiomers. (+)(R)- thalidomide is a sedative, but (-)(S)-thalidomide is a teratogen (i.e., a drug which can harm a fetus in the womb). (-)(S)-thalidomide inhibits new blood vessel growth. This is detrimental to a fetus because new blood vessels provide a road map for the growth of limbs and organs during the development of a fetus. Thus, (-)(S)-thalidomide is the unwanted enantiomer and needs to be separated.

In this chapter, we are concerned with the separation of deformable vesicle-like enantiomers by a specific flow pattern generated by surface acoustic waves (SAWs) [29].

In particular, we consider an IDT (Figure 4.2) built into a circuit board on top of which a frame of plexiglas (PMMA) is glued to form a miniature trough (cf. Figure 4.3 (left)). Figure 4.3 (right) shows a schematic side view of the setup with

the IDT on the bottom of the trough, a reservoir of water on top, and a particle floating on the surface. Applying an alternating frequency then drives the streaming and generates the scenario sketched in Figure 4.4.

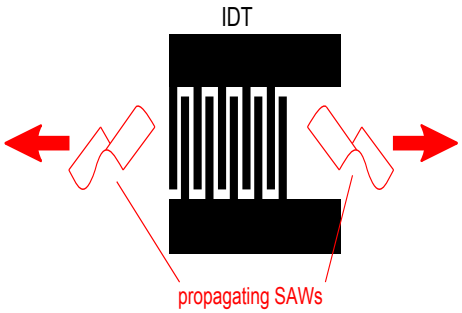

Figure 4.2: *Left:* Interdigital tranducer (IDT) for generation of SAWs

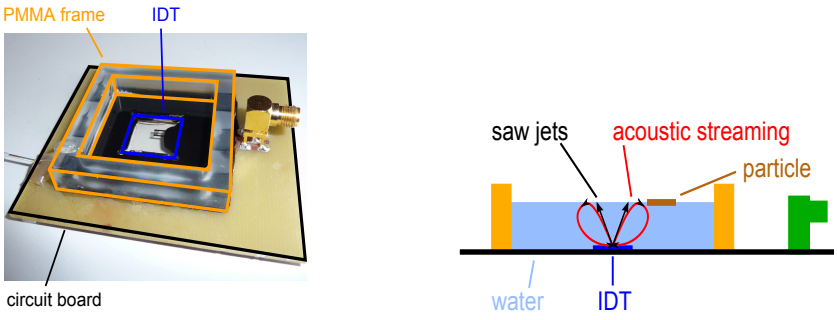

Figure 4.3: *Left:* Photograph of the experimental setup for the investigation of the behavior of chiral objects in quadripolar microflows. *Right:* Schematic side view of the experimental setup.

Almost flat L-shaped hydrophobic enantiomers are injected onto the surface of the fluid between two counter-rotating vortices. The result is that right-handed (left-handed) enantiomers get trapped by left-rotating (right-rotating) vortices in the sense that they stably rotate around the center of the vortex.

In section 4.1, we present a mathematical model for the separation of deformable vesicle-like enantiomers with SAW-generated vortices. Section 4.3 is devoted to the results of numerical simulations.

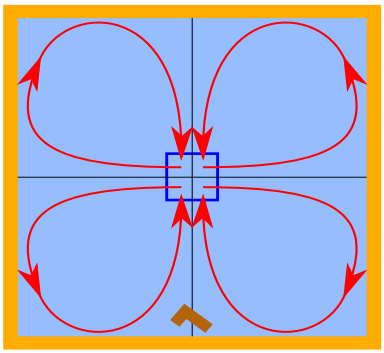

Figure 4.4: Schematic top view of the experimental setup

4.1 Mathematical model

For the modeling and numerical simulation of the surface acoustic wave actuated enantiomer separation we use the Finite Element-Immersed Boundary Method (FE-IB) discussed in the previous chapters.

4.1.1 Generation of the vorticity patterns by SAWs

The SAWs are generated by an IDT as in subsection 3.1.1 of chapter 2.3. We assume a container filled with fluid is placed on top a piezoelectric material with density ρ_p and spatial domain Ω_1 with boundary $\Gamma_1 = \partial\Omega_1$. Further, we suppose that the fluid in the container occupies a domain $\Omega_2 := (0, L)^2 \times (0, H), H,\ L > 0$, with boundary $\Gamma_2 := \Gamma_b \cup \Gamma_l \cup \Gamma_s$, where $\Gamma_b := (0, L) \times (0, L) \times \{0\},\ \Gamma_s := (0, L) \times (0, L) \times \{H\}$, and $\Gamma_l := \Gamma_2 \setminus (\Gamma_b \cup \Gamma_s)$. The impact of the SAWs on the fluid flow is realized through a boundary condition on $\Gamma_{SAW} := [L/2 - a, L/2 + a]^2 \times \{0\}, a > 0$.

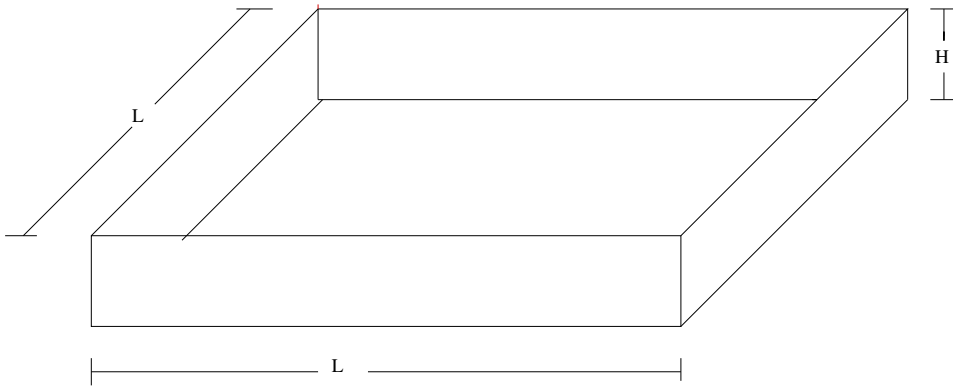

Figure 4.5: Fluid container

Denoting by ρ_f, η, ξ the density, the standard and the bulk viscosity of the fluid and by $\mathbf{v}, p$ the velocity and the pressure, the fluid flow is described by the compressible Navier-Stokes equations

$$\rho_f\big(\frac{\partial \mathbf{v}}{\partial t} + \mathbf{v}\cdot\nabla\mathbf{v}\big) = \nabla\cdot\boldsymbol{\sigma} \quad \text{in } Q_2 := \Omega_2\times(0,T), \tag{4.1a}$$

$$\frac{\partial \rho_f}{\partial t} + \nabla\cdot(\rho_f\mathbf{v}) = 0 \qquad \text{in } Q_2, \tag{4.1b}$$

$$\mathbf{v}(\cdot,t) = \frac{\partial \mathbf{u}}{\partial t}(\cdot,t) \quad \text{on } \Gamma_{SAW}\ ,\ t\in(0,T), \tag{4.1c}$$

$$\mathbf{v}(\cdot,t) = \mathbf{0} \quad \text{on } (\Gamma_b\setminus\Gamma_{SAW})\cup\Gamma_l\ ,\ t\in(0,T), \tag{4.1d}$$

$$\boldsymbol{\sigma}\mathbf{n} = \mathbf{0} \quad \text{on } \Gamma_s\ ,\ t\in(0,T)\ , \tag{4.1e}$$

$$\mathbf{v}(\cdot,0) = \mathbf{0}, \quad p(\cdot,0) = 0 \quad \text{in } \Omega_2, \tag{4.1f}$$

where the constitutive equation for the stress tensor $\boldsymbol{\sigma} = (\sigma_{ij})_{i,j=1}^3$ reads

$$\sigma_{ij} := -p\ \delta_{ij} + 2\eta\varepsilon_{ij}(\mathbf{v}) + \delta_{ij}(\xi - 2\eta/3)\nabla\cdot\mathbf{v}. \tag{4.1g}$$

Here, ρ_f is the density of the fluid, $\varepsilon = (\varepsilon_{ij})_{i,j=1}^3,\ \varepsilon_{ij} := (\partial v_i/\partial x_j + \partial v_j/\partial x_i)/2$ stands for the rate of deformation tensor, and $\mathbf{u}$ denotes the mechanical displacement of the

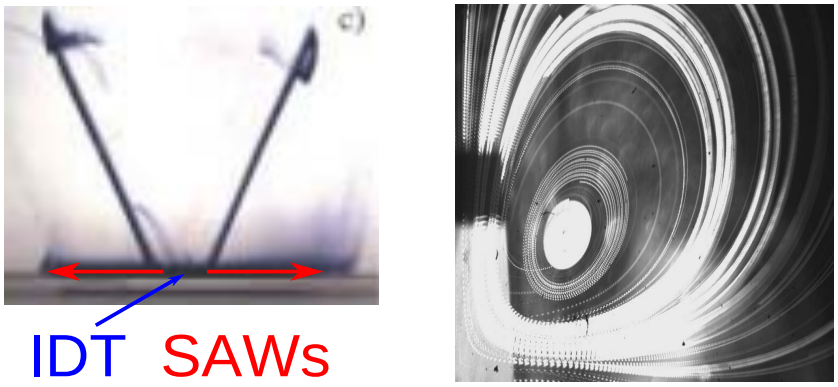

Figure 4.6: *Left:* An IDT with a dye on top is placed on the bottom of a trough. The generated SAWs couple into the fluid and form two jets. *Right:* Vorticity pattern (acoustic streaming) in the upper right quadrant of the surface of the fluid.

wall of the container caused by the SAWs and obtained by solving the linearized piezoelectric equations (3.4) in Ω_1.

Remark 4.1.1. We have to consider the compressible Navier-Stokes equations, since the propagation of acoustic waves in the fluid causes compressible effects.

The SAW-induced fluid flow exhibits two different time scales. When the SAWs enter the fluid filled microchannels, sharp jets are created within nanoseconds (cf. Figure 4.6 (left)). The SAWs propagate upwards and experience a significant damping which results in a vorticity flow pattern called acoustic streaming (cf. Figure 4.6 (right)) . This relaxation process happens on a time scale of milliseconds. The multiscale character can be appropriately taken care of by a homogenization approach. According to [2], we introduce a scale parameter $0 < \epsilon \ll 1$ which represents the maximum deflection of the walls of the microchannels, and we consider the asymptotic

expansions

$$\begin{aligned}\rho_f &= \rho_{f,0} + \epsilon\rho_f' + \epsilon^2\rho_f'' + \mathcal{O}(\epsilon^3),\\ \mathbf{v} &= \mathbf{v}_0 + \epsilon\mathbf{v}' + \epsilon^2\mathbf{v}'' + \mathcal{O}(\epsilon^3),\\ p &= p_0 + \epsilon p' + \epsilon^2 p'' + \mathcal{O}(\epsilon^3).\end{aligned}$$

We assume that $\mathbf{v}_0 \equiv \mathbf{0}$ and $p_0 \equiv 0$, (i.e., fluid is at rest if no SAW actuation) and take $\rho_{f,0}$ to be the density of the carrier fluid. Then, collecting all first order terms and setting $\rho_{f,1} := \epsilon\rho_f'$, $\mathbf{v}_1 := \epsilon\mathbf{v}'$, $p_1 := \epsilon p'$, a simple calculation reveals that the triple $(\rho_{f,1}, \mathbf{v}_1, p_1)$ satisfies the following initial-boundary value problem for a linear system a time-periodic boundary condition on Γ_{SAW} :

$$\rho_{f,0}\frac{\partial \mathbf{v}_1}{\partial t} - \nabla\cdot\boldsymbol{\sigma}_1 = \mathbf{0} \qquad \text{in } \Omega_2\times(0,T_1], \tag{4.2a}$$

$$\frac{\partial \rho_{f,1}}{\partial t} + \rho_{f,0}\nabla\cdot\mathbf{v}_1 = \mathbf{0} \qquad \text{in } \Omega_2\times(0,T_1], \tag{4.2b}$$

$$\mathbf{v}_1 = \frac{\partial \mathbf{u}}{\partial t} \qquad \text{on } \Gamma_{SAW}\times(0,T_1], \tag{4.2c}$$

$$\boldsymbol{\sigma}_1\mathbf{n} = 0 \qquad \text{on } \Gamma_s\times(0,T_1], \tag{4.2d}$$

$$\mathbf{v}_1(\cdot,t) = 0 \qquad \text{on } (\Gamma_b\setminus\Gamma_{SAW})\cup\Gamma_l,\ t\in(0,T_1], \tag{4.2e}$$

$$\mathbf{v}_1(\cdot,0) = \mathbf{0}\ ,\ p_1(\cdot,0) = 0, \qquad \text{in } \Omega_2, \tag{4.2f}$$

with the constitutive equations

$$\boldsymbol{\sigma}_1 = ((\sigma_1)_{ij}),\ (\sigma_1)_{ij} := -p_1\delta_{ij} + 2\eta\varepsilon_{ij}(\mathbf{v}_1) + \delta_{ij}(\xi - 2\eta/3)\nabla\cdot\mathbf{v}_1, \tag{4.2g}$$

$$p_1 = c_0^2\rho_{f,1}. \tag{4.2h}$$

Here, $T_1 := 2\pi/\omega$, where ω is the angular frequency of the time harmonic SAW excitation, $\partial\mathbf{u}/\partial t$, and c_0 stands for the small signal sound speed in the fluid. The

system (4.2) describes the propagation of the SAW in the fluid filled container. Next, collecting all terms of order $O(\epsilon^2)$, neglecting time derivatives, and performing the time-averaging

$$\langle w \rangle := \frac{1}{T} \int_{t_0}^{t_0+T_1} w \; dt,$$

we arrive at

$$-\nabla \cdot \boldsymbol{\sigma}_2 = \langle -\rho_{f,1} \frac{\partial \mathbf{v}_1}{\partial t} - \rho_{f,0} [\nabla \mathbf{v}_1] \mathbf{v}_1 \rangle \qquad \text{in } \Omega_2, \tag{4.3a}$$

$$\rho_{f,0} \nabla \cdot \mathbf{v}_2 = \langle -\nabla \cdot (\rho_{f,1} \mathbf{v}_1) \rangle \qquad \text{in } \Omega_2, \tag{4.3b}$$

$$\mathbf{v}_2 = -\langle [\nabla \mathbf{v}_1] \mathbf{u} \rangle \qquad \text{on } \Gamma_{SAW}, \tag{4.3c}$$

$$\mathbf{v}_2 = \mathbf{0} \qquad \text{on } (\Gamma_b \setminus \Gamma_{SAW}) \cup \Gamma_l, \tag{4.3d}$$

$$\mathbf{n} \cdot \mathbf{v}_2 = 0 \qquad \text{on} \Gamma_s, \tag{4.3e}$$

$$\mathbf{n} \cdot \boldsymbol{\sigma}_2 \boldsymbol{\tau}_i = 0 \qquad \text{on } \Gamma_s, \; 1 \leq i \leq 2, \tag{4.3f}$$

with

$$\boldsymbol{\sigma}_2 = ((\sigma_2)_{ij}), \; (\sigma_2)_{ij} := -p_2 \delta_{ij} + 2\eta \varepsilon_{ij}(\mathbf{v}_2) + \delta_{ij}(\xi - 2\eta/3) \nabla \cdot \mathbf{v}_2, \tag{4.3g}$$

$$p_2 = c_0^2 \rho_{f,2}. \tag{4.3h}$$

Here, $\boldsymbol{\tau} = (\boldsymbol{\tau}_1, \boldsymbol{\tau}_2)^T$ is the unit tangential vector on Γ_s. We note that (4.3e),(4.3f) are the free slip boundary conditions on the surface of the fluid. The compressible Stokes system (4.3) is used as a model for the acoustic streaming flow pattern. For the formulations of equations (4.2) and (4.3) and further discussion, we refer to [2, 30].

4.1.2 Fluid and immersed boundary equations

Since the enantiomers float on the surface Γ_s of the fluid, we are only interested in the fluid flow and the motion of the enantiomers on Γ_s. The fluid flow on Γ_s can be modeled by the incompressible Navier-Stokes equations with a source term $\mathbf{f} = \mathbf{f}_q + \mathbf{f}_g$, (where $\mathbf{f}_q$ is a quadrupolar force density reflecting the SAW induced vorticity pattern on Γ_s, and $\mathbf{f}_g$ is a global force density, reflecting the impact of the enantiomers on the flow):

$$\rho_f \frac{\partial \mathbf{v}}{\partial t} + \rho_f(\mathbf{v}\cdot\nabla)\mathbf{v} - \eta\Delta\mathbf{v} + \nabla p = \mathbf{f} \quad \text{in } \Gamma_s \times (0,T), \tag{4.4a}$$

$$\nabla\cdot\mathbf{v} = 0 \quad \text{in } \Gamma_s \times (0,T), \tag{4.4b}$$

$$\mathbf{v} = \mathbf{0} \quad \text{on } \partial\Gamma_s \times (0,T), \tag{4.4c}$$

The quadrupolar force density is given according to

$$\mathbf{f}_q := -\eta\Delta\hat{\mathbf{v}},\ \hat{\mathbf{v}} = (\hat{v}_1, \hat{v}_2)^T,\ \hat{v}_1 = \partial\Psi/\partial x_2,\ \hat{v}_2 = -\partial\Psi/\partial x_1 \tag{4.5}$$

where Ψ is a stream function described as

$$\Psi(x_1, x_2) = v_0(f)\frac{L\sqrt{3}}{\pi}\ \frac{\sin(\pi x_1/L)\sin(\pi x_2/L)}{(2-\cos(\pi x_1/L))(2-\cos(\pi x_2/L))}. \tag{4.6}$$

Here, $v_0(f) > 0$ stands for a parameter that depends on the operating frequency f of the IDT and is fitted to available experimental data [10].

In the FE-IB, an immersed enantiomer is modeled as a body consisting of an elastic membrane enclosing a fluid which here is assumed to have the same density and viscosity as the carrier fluid in the container. Using notations from previous

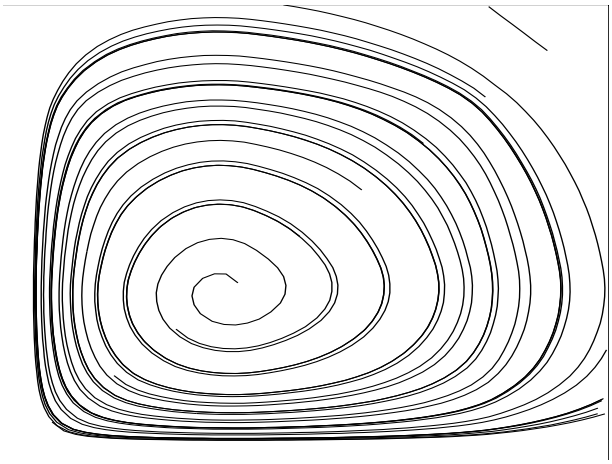

Figure 4.7: Simulation of SAW-generated vortices

chapters, the immersed enantiomer is assumed to occupy a subdomain $B_t \subset \Gamma_s, t \in [0,T]$, with boundary ∂B_t which is a non-selfintersecting closed curve. We further assume that the boundary ∂B_0 of the initial configuration B_0 has length $\ell := |\partial B_0|$ and denote by $\bar{q} \in [0,\ell]$ the Lagrangian coordinate labeling a material point on ∂B_0. We refer to $\mathbf{X}(\bar{q},t) = (X_1(\bar{q},t), X_2(\bar{q},t))^T$ as the position vector at time $t \in (0,T]$ which moves with the velocity $\mathbf{v}$ of the fluid such that the equation of motion takes the form

$$\frac{d\mathbf{X}}{dt}(\bar{q},t) = \mathbf{v}(\mathbf{X}(\bar{q},t),t), \quad \bar{q} \in [0,\ell],\ t \in [0,T], \tag{4.7a}$$

$$\mathbf{X}(\bar{q},0) = \mathbf{X}^0(\bar{q}), \quad \bar{q} \in [0,\ell], \tag{4.7b}$$

where $\mathbf{X}^0$ stands for the initial position.

Denoting by $\mathbf{F}$ the local force density according to $\mathbf{F}(\bar{q},t) = -E'(\mathbf{X}(\bar{q},t))$, where E' is the Gâteaux derivative of E, the global force density $\mathbf{f}_g$ is given by

$$\langle \mathbf{f}_g(t), \mathbf{w} \rangle_{\mathbf{H}^{-1},\mathbf{H}_0^1} = \int_0^\ell \mathbf{F}(\bar{q},t) \cdot \mathbf{w}(\mathbf{X}(\bar{q},t))\, d\bar{q}, \quad \mathbf{w} \in \mathbf{H}_0^1(\Gamma_s). \tag{4.8}$$

where $\mathbf{F}$ is described according to equation (3.13).

4.2 Discretization

The discretization of the variational equations associated to (2.1) is done as in chapter 2.3 subsection 3.1.4, where we discretized the incompressible Navier-Stokes equations using the Taylor-Hood P2/P1 elements in space and the backward Euler scheme in time. On the other hand, we have discretized the immersed body using cubic splines in space and the forward Euler method in time.

Remark 4.2.1. In practice, for the formulation of the discrete bending energy $E_h^b(t)$ we use equation (3.42). In particular, for the L-shaped enantiomers, $E_h^b(t)$ is given according to

$$E_h^b(t) \approx \frac{1}{2}\sum_{i=1}^{M} \kappa_p \kappa_b \left(\frac{\tan(\alpha_i(t)-\alpha_d)/2)}{2\Delta\bar{q}}\right)^2 \Delta\bar{q}.$$

where α_i is the angle between the vectors $(\mathbf{X}_{i+1}-\mathbf{X}_i)(t)$ and $(\mathbf{X}_i-\mathbf{X}_{i-1})(t)$ and the desired angle $\alpha_d = \pi/2$ for corner nodes and 0 otherwise. Further κ_p is a 'penalty' coefficient which is assumed to have a value greater than one at corner nodes to guarantee less deformation.

4.3 Numerical simulations

We present the results of numerical simulations of the separation of deformable, initially L-shaped enantiomers by SAW-generated vorticity patterns consisting of

four pairwise counter-rotating vortices at the surface of the fluid. The material data and the numerical data have been chosen as follows:

Material Data: As piezoelectric material we have used 128^o rotated **YX** lithium niobate ($LiNbO_3$) with density $\rho_p = 4.63 \cdot 10^3\ kg/m^3$ and elasticity tensor $\mathbf{c}$, piezoelectric tensor $\mathbf{e}$, and dielectric tensor $\boldsymbol{\epsilon}$ given in Table 4.1. The operating frequency f of the IDT has been chosen according to $f = 1.42 \cdot 10^2\ MHz$. Based on experimental measurements, we found out that $v_0(f) = 2.0.10^{-3} m/s$ in (4.6) provides a good approximation of the resulting vorticity pattern at the surface of the fluid.

$\mathbf{c}$ $[10^{10}\frac{\mathbf{N}}{\mathbf{m^2}}]$	c_{11} 20.3	c_{12} 5.3	c_{13} 7.5	c_{14} 0.9	c_{33} 24.5	c_{44} 6.0	c_{66} 7.5
$\mathbf{e}$ $[\frac{\mathbf{C}}{\mathbf{m^2}}]$	$e_{15} = e_{24}$ 3.7		$e_{22} = -e_{21}$ 2.5		$e_{31} = e_{32}$ 0.1		e_{33} 1.3
$\boldsymbol{\epsilon}$ $[10^{-12}\frac{\mathbf{F}}{\mathbf{m}}]$	$\epsilon_{11} = \epsilon_{22}$ 749.0				ϵ_{33} 253.2		

Table 4.1: Material Moduli for 128^o rotated **YX** $LiNbO_3$ (note that $c_{11} = c_{22}, c_{13} = c_{23}, c_{14} = -c_{24} = c_{56}, c_{44} = c_{55}$ and $e_{22} = -e_{16}$)

The fluid with density $\rho_f = 1.1 \cdot 10^3\ kg/m^3$ and viscosity $\eta = 1.01 \cdot 10^{-6}\ m^2/s$ occupied a domain $\Omega_2 = (0, L)^2 \times (0, H)$ with $L = 4.0.10^{-2}$ m and $H = 5.0.10^{-3}$ m. We considered L-shaped enantiomers of perimeter $5.0.10^{-4} m$. The material moduli of the enantiomers are given by $\kappa_e = 3.0.10^{-2}\ N/m$ and $\kappa_b = 2.5.10^{-17}\ Nm$. Further, we took $\kappa_p = 1.5$ at the corner nodes.

Numerical Data: For the numerical solution of the coupled system by the Backward Euler/Forward Euler FE-IB we have used a uniform simplicial triangulation of Γ_s by right isosceles with $h = L/35$ and a uniform partition of $[0, \ell]$ with $\Delta q = \ell/200$.

We have further used a uniform partition of the time interval with time step size $\Delta t = 1/9000$ satisfying the CFL-condition (3.52).

Simulation Results: An initially L-shaped, left-handed enantiomer has been injected onto the surface of the fluid approximately in the middle between two counter-rotating vortices. The motion of the enantiomer is such that it gets attracted by the right-rotating fluid vortex. After the completion of the first cycle around the center of the vortex, new cycles begin with paths of the enantiomer similar to the first one (cf. Figure 4.8). Figure 4.9 displays the paths of an initially L-shaped, right-handed enantiomer which gets attracted by the left-rotating vortex. The separation does not depend on the position of the enantiomers with respect to the velocity field (see Figure 4.11 for a left-handed L-shaped enantiomer rotated by 90° compared to the upright position). However, for a proper separation of the enantiomers it is important that they are injected approximately in the middle between two counter-rotating vortices.

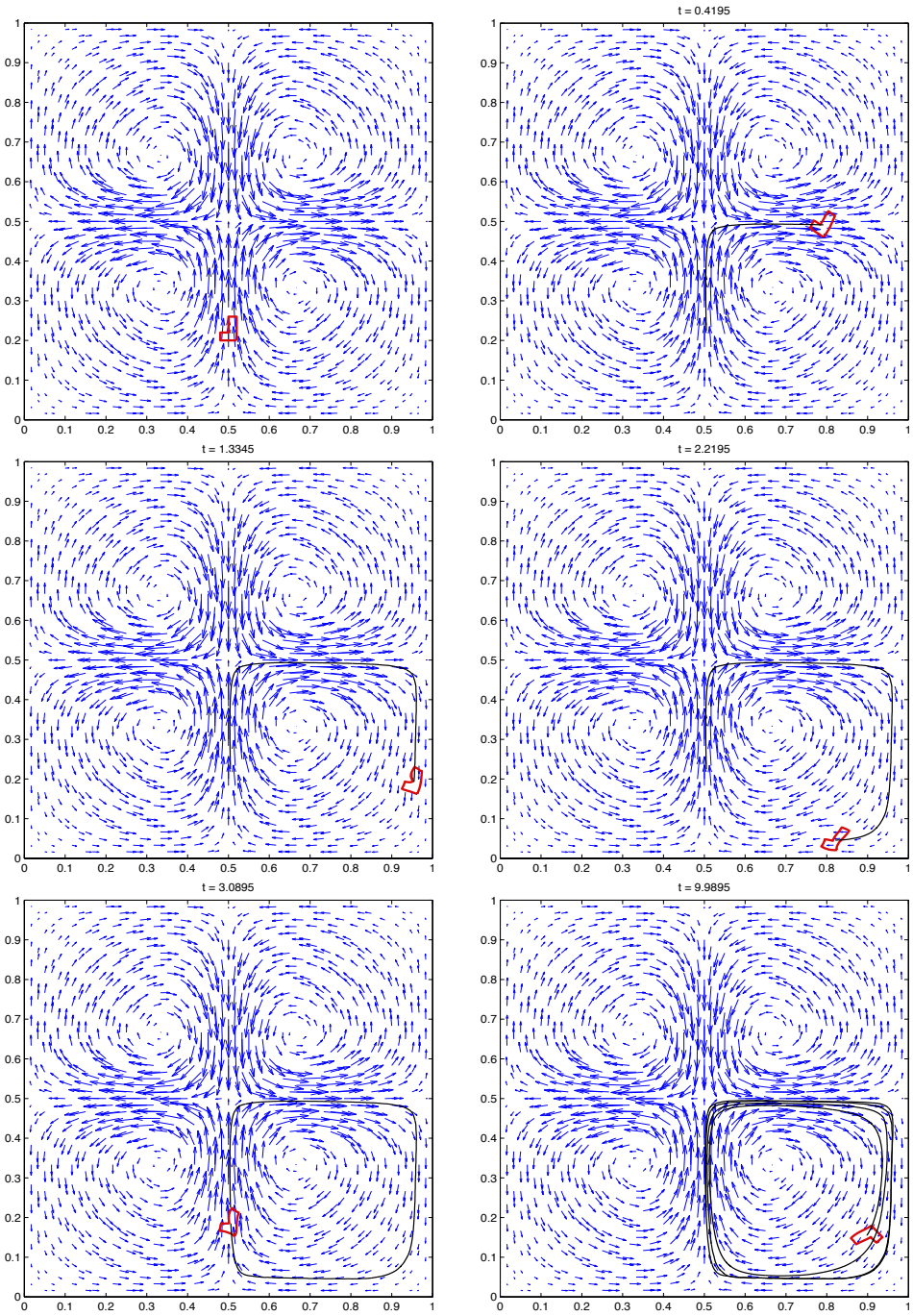

Figure 4.8: Velocity field and motion of a left-handed L-shaped enantiomer initially placed in the middle between two counter-rotating vortices

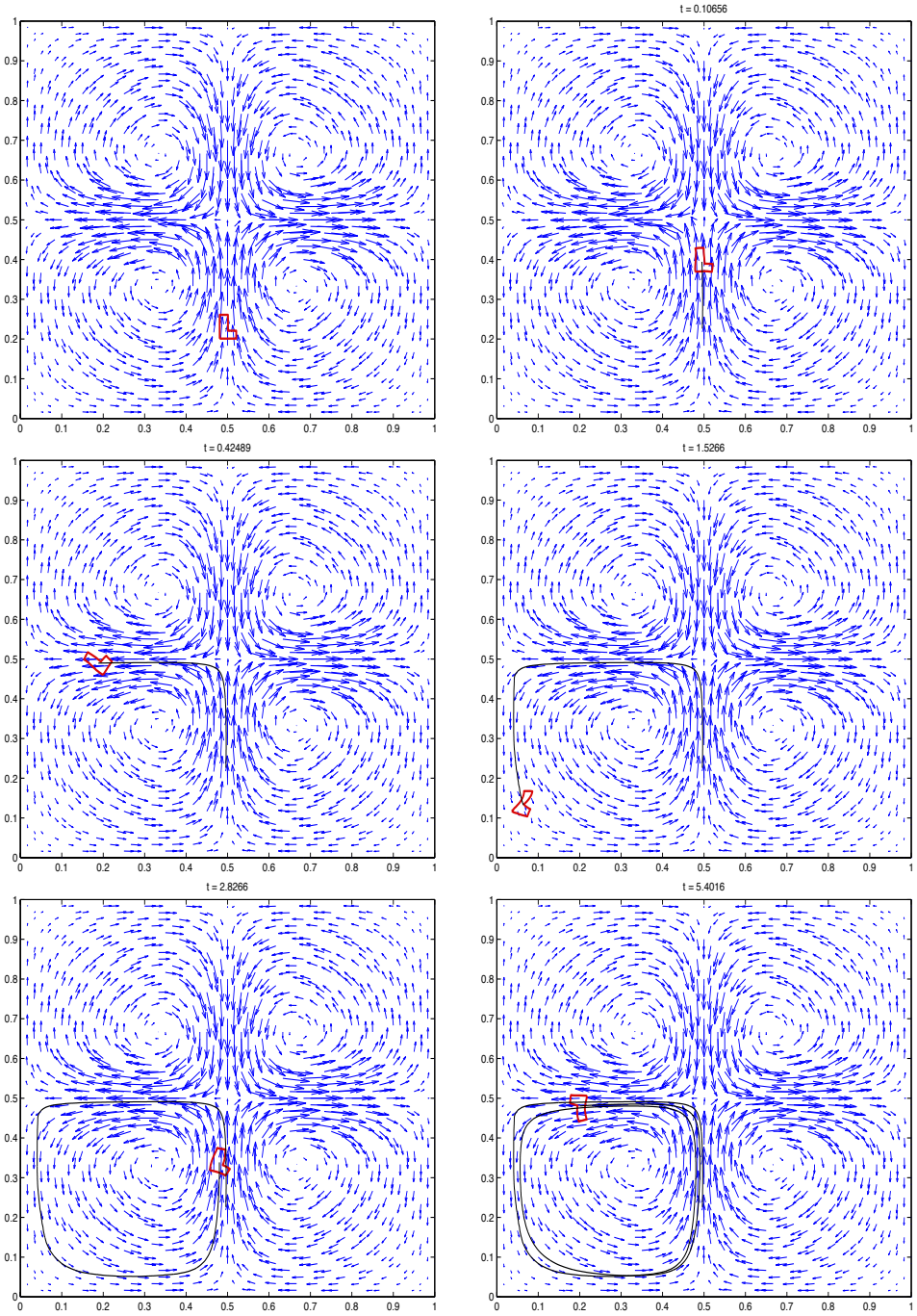

Figure 4.9: Velocity field and motion of a right-handed L-shaped enantiomer initially placed in the middle between two counter-rotating vortices

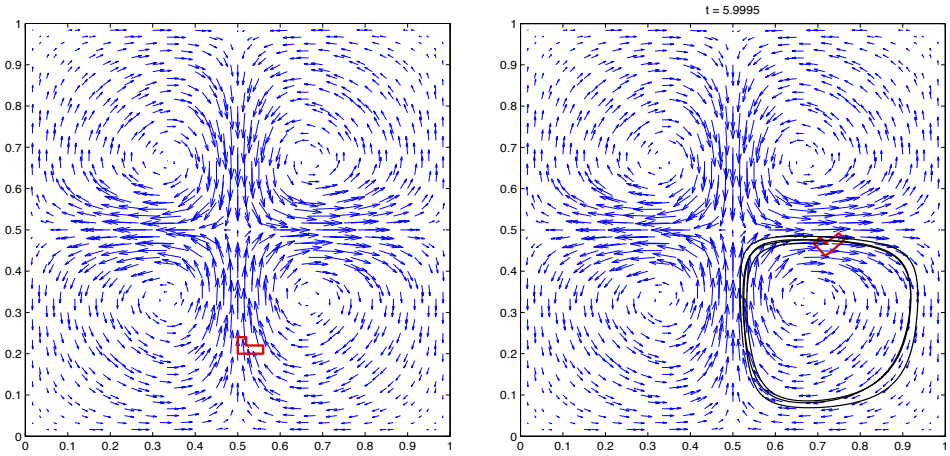

Figure 4.10: Velocity field and motion of a left-handed L-shaped enantiomer rotated by 90° with respect to the upright position

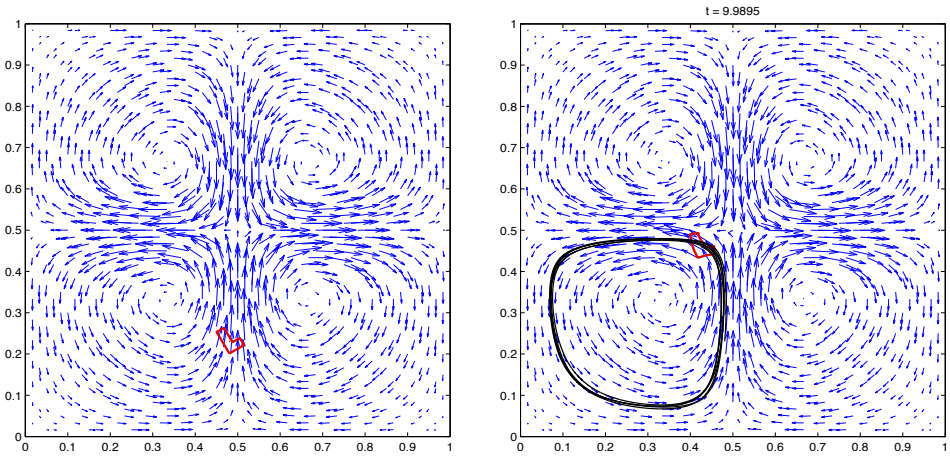

Figure 4.11: Velocity field and motion of a right-handed L-shaped enantiomer rotated by 30° with respect to the upright position

In [10], the numerical simulation of the separation of rigid L-shaped enantiomers has been considered based on the Fictitious Domain Lagrange Multiplier (FDLM) method from [26].

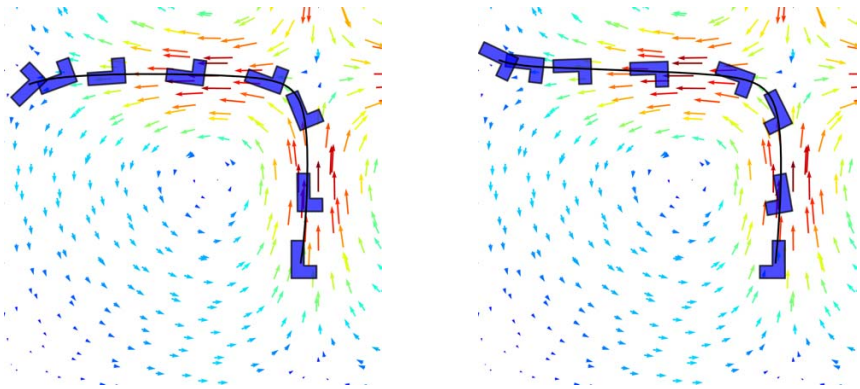

Figure 4.12: Left: Attraction of a right-handed L-shaped enantiomer by the counter clockwise rotating vortex in the lower left quadrant. Right: Attraction of a left-handed L-shaped enantiomer by the clockwise rotating vortex in the upper left quadrant

Figure 4.12 displays the motion of a right-handed and a left-handed L-shaped enantiomer initially placed slightly left of the middle between the two counter rotating vortices in the lower quadrants of the surface of the fluid. As can be seen in Figure 4.12 (left), the right-handed enantiomer gets attracted by the counter clockwise rotating vortex in the lower left quadrant. On the other hand, as shown in Figure 4.12 (right), the right-handed enantiomer follows a trajectory that leads to a path around the center of the clockwise rotating vortex in the upper right quadrant. Likewise, Figure 4.13 shows that a right-handed (left-handed) enantiomer initially placed a little bit to the right of the middle between the two counter rotating vortices gets attracted by the counter clockwise (clockwise) rotating vortex in the upper right (lower right) quadrant.

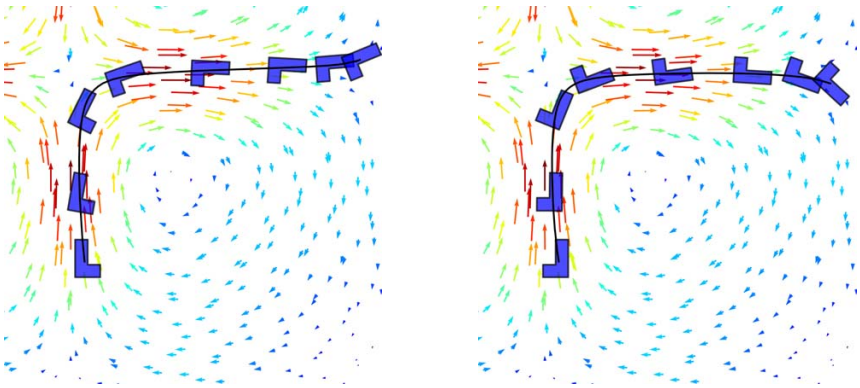

Figure 4.13: Left: Attraction of a right-handed L-shaped enantiomer by the counter clockwise rotating vortex in the upper right quadrant. Right: Attraction of a left-handed L-shaped enantiomer by the clockwise rotating vortex in the lower right quadrant

When we compare the results of the application of the FE-IB method and the FDLM method, we see that in both cases right-handed (left-handed) enantiomers get attracted by left-rotating (right-rotating) vortices, i.e., in both cases we can achieve perfect separation. In detail, however, there are slight differences in so far as in the FE-IB-based simulation a right-handed (left-handed) L-shaped enantiomer follows a path around the center of the left-rotating (right-rotating) vortex in the lower left (lower right) quadrant of the surface of the fluid, whereas in the FDLM method a right-handed (left-handed) enantiomer gets attracted by the left-rotating (right-rotating) vortex in the upper right (upper left) quadrant when the initial position is slightly right (left) of the middle of the two counter-rotating vortices in the lower half of the surface of the fluid. This can be explained by the fact that in the FDLM method the inertia of the enantiomers is taken into account while it is not in the FE-IB method.

CHAPTER 6

Conclusions and Future Work

Particle sorting in a sample is a growing need in many applications, including basic cell biology, cancer research, clinical diagnostics, tissue engineering, and drug design in pharmacology. In the past, many techniques have been investigated for this purpose. Most of the methodologies depend heavily on different properties of the particles in the sample, such as density, size, charge, or polarization. Hence they are restricted to specific applications. A new tehchnology is surface acoustic wave actuated particle sorting, which doesn't depend on such contrasts.

In this dissertation, we have provided mathematical models and numerical simulations for surface acoustic wave-actuated cell sorting, as well as enantiomer separation

using surface acoustic wave generated vorticity patterns. This is accomplished using the Finite Element Immersed Boundary (FE-IB) method. The FE-IB method couples the Navier-Stokes equations for modeling the incompressible fluid flow and elasticity equations for the description of the force exerted by the immersed body on the fluid. The surface acoustic waves (SAWs) are generated using an interdigital transducer (IDT), and their action on the fluid is realized through boundary conditions of the fluid equations. Stability estimates for the problem under the given boundary conditions has been established.

For SAW-actuated cell sorting, we considered a separation channel with three inlets and two outlets placed on top of a plastic chip partially coated with a piezoelectric substrate, with an IDT paced close to it. We have presented the numerical simulation of the sorting of a red blood cell and a melanoma breast cancer. Our simulations agree with experimentally obtained results [20].

On the other hand, for the separation of enantiomers, a quadrupolar force density is used to simulate the SAW-generated vorticity patterns. The numerical simulations show that these patterns reproduce the acoustic streaming generated by SAWs in experiment [10]. We have tested the technique for the separation of deformable vescile-like L-shaped enantiomers. Our results show a perfect separation when the enantiomers are injected in the middle of two counter rotating vortices. We have further compared our results with current simulations done for rigid L-shaped enantiomers, using the fictitous domain technique, and found out that our results agree [10].

In SAW-actuated particle sorting, the experimental design relies on a heuristic

fine tuning of the aperture of the IDT (determining the direction of the SAW) and its operating frequency on one hand and the inflow velocity at the inlets on the other hand. Thus there is a need for a rigorous, mathematically founded design based on the optimal control of the underlying state equations describing the generation of acoustic streaming, and the motion of the cells or enantiomers in the SAW manipulated carrier fluid. Therefore, subsequent research might investigate the optimal control of these problems. All of our simulations are done in $\mathbb{R}^2$, hence a natural continuation to this work is to consider the problems in $\mathbb{R}^3$.

APPENDIX A

Computation of the shape of the red blood cell (RBC)

RBC assumes a biconcave disc shape which permits its passage through capillaries and enables its surface to volume ratio to be significantly higher than that of a sphere. The RBC membrane is modeled as a flexible two-dimensional thin structure enclosing an incompressible fluid, using a Lagrangian description. The shape of a RBC is determined by the elasticity properties of the membrane and its so called reduced volume, which we explain as follows. Given a circle of radius r and volume V_c. If we shrink the volume of the circle and keep it's perimeter nearly constant, we get a reduced volume denoted by V_r. We further denote by $C_r := V/V_c$ the *reduced ratio*.

For the computation of the shape of the RBC we prescribe its initial or static shape according to (cf. [35])

$$y = 1/2[1 - x^2]^{1/2}(a_0 + a_1 x^2 + a_2 x^4),\ x \in [-1, 1], \tag{A.1}$$

where a_0, a_1 and a_2 are constants obtained from experiments. Then we determine the perimeter P of the given resting membrane to calculate the radius r of the circle with the same perimeter. We define the desired volume of the RBC as $V_d := C_r V_c = C_r \pi r^2$. Then to the energy functional defined in (3.12), we add the term

$$E_p := \frac{\kappa_p}{2}\left(\frac{V(\mathbf{X}) - V_d}{V_d}\right) \tag{A.2}$$

E_p is a penalty term that enforces the change in volume, $V(\mathbf{X})$, of the membrane to approach V_d. To achieve this, we set the force acting on $\mathbf{X}_\ell$ at time t as

$$\mathbf{F}_\ell = -\Big(\frac{\partial E(t)}{\partial \mathbf{X}_\ell} + \frac{\partial E_p(t)}{\partial \mathbf{X}_\ell}\Big), 1 \le \ell \le M \tag{A.3}$$

and solve the following equation of motion so that the total energy is minimum. (cf. [48, 49])

$$m_{\partial B}\ddot{\mathbf{X}}_\ell(t) + \mu_{\partial B}\dot{\mathbf{X}}_\ell(t) = \mathbf{F}_\ell,\ 1 \le \ell \le M. \tag{A.4}$$

where $m_{\partial B}$ and $\mu_{\partial B}$ denote the mass and viscosity of the RBC membrane respectively. A second-order accurate scheme yields

$$\mathbf{X}_\ell(t + \Delta t) = \frac{\Delta^2 \mathbf{F}_\ell + 2m_{\partial B}\mathbf{X}_i(t) + (\mu_{\partial B}\Delta t/2 - m_{\partial B})\mathbf{X}_\ell(t - \Delta t)}{m_{\partial B} + \mu_{\partial B}\Delta t/2} \tag{A.5}$$

$1 \le \ell \le M$, with $\mathbf{X}_i(0 - \Delta t) := \Delta \mathbf{X}_\ell(0)$ for solving the equation.

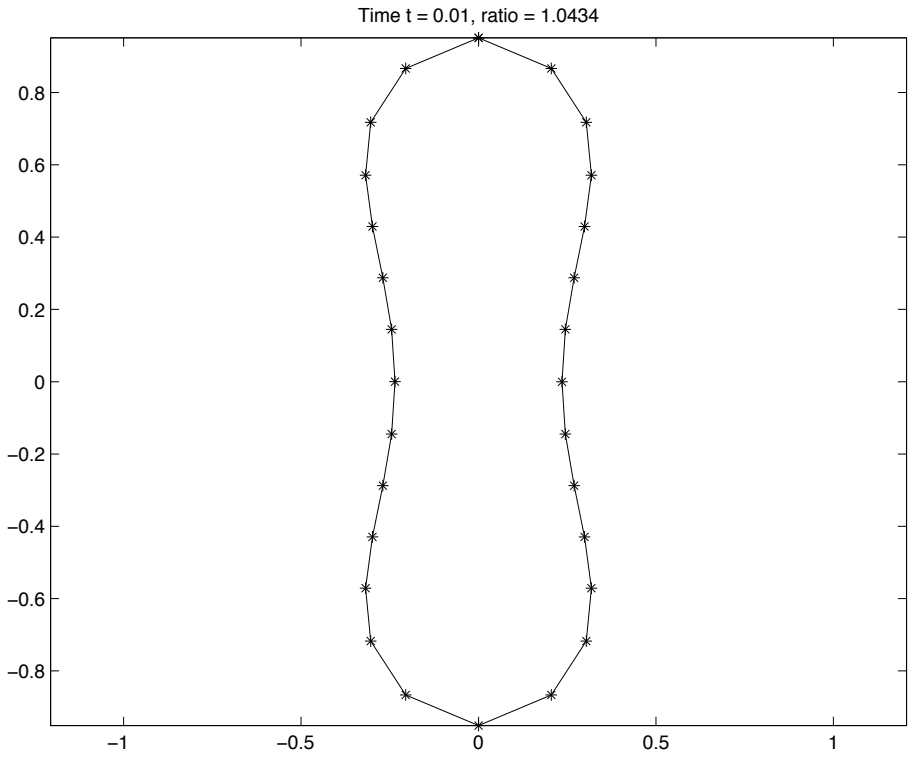

Figure A.1: Shape of an RBC

APPENDIX B

Notation and symbols

$\mathbb{R}$	Set of real numbers
SAW	Surface acoustic wave
IDT	Interdigital transducer
BioMEMS	Biological micro-electro-mechanical system
FE-IB	Finite element immersed boundary
Ω	a bounded polygonal domain in $\mathbb{R}^2$
$\Gamma = \partial\Omega$,	boundary of Ω
$L^2(\Omega)$	Scalar and vector-valued square Lebesgue integrable functions on Ω
$\mathbf{L}^2(\Omega)$	Vector-valued square Lebesgue integrable functions on Ω

$(\cdot,\cdot)_{0,\Omega}$	Inner prodcut of the space $L^2(\Omega)$ or $\mathbf{L}^2(\Omega)$
$\|\cdot\|_{0,\Omega}$	Norm of the space $L^2(\Omega)$ or $\mathbf{L}^2(\Omega)$
$L^2_0(\Omega)$	Scalar square labesgue interable of functions with zero integral mean
$H^s(\Omega)$	Sobolev spaces of scalar -valued functions
$\mathbf{H}^s(\Omega)$	Sobolev spaces vector-valued functions
$(\cdot,\cdot)_{s,\Omega}$	Inner product of $H^s(\Omega)$ or $\mathbf{H}^s(\Omega)$
$\|\cdot\|_{s,\Omega}$	Norm of $H^s(\Omega)$ or $\mathbf{H}^s(\Omega)$
$C^\infty_0(\Omega)(\mathcal{D})$	The space of inifinitely differentiable scalar functions with compact support
$\mathbf{C}^\infty_0(\Omega)(\boldsymbol{\mathcal{D}})$	The space of inifinitely differentiable vector valued functions with compact support
$H^s_{0,\Gamma'}(\Omega)$	Closure of $C^\infty_{0,\Gamma'}(\Omega)$ in $H^1(\Omega)$ for $\Gamma' \subset \Gamma$
$\mathbf{H}^s_{0,\Gamma'}(\Omega)$	Closure of $\mathbf{C}^\infty_{0,\Gamma'}(\Omega)$ in $\mathbf{H}^1(\Omega)$ for $\Gamma' \subset \Gamma$
$H^{-s}(\Omega)$	Dual space of $H^s_0(\Omega)$
$\mathbf{H}^{-s}(\Omega)$	Dual spaces $\mathbf{H}^{-s}(\Omega)$
V^*	Dual spaces of $V \subset H^1(\Omega)$
$\langle\cdot,\cdot\rangle_{V^*,V}$	Dual product
$H^{s-1/2}(\Gamma')$	Trace space of functions in $H^s(\Omega)$
$\mathbf{H}^{s-1/2}_{00}(\Gamma')$	Spaces of functions whose extensions by zero to $\Gamma \setminus \Gamma'$ belong to $H^{s-1/2}(\Gamma)$

Bibliography

[1] B. Alberts, A. Johnson, J. Lewis, M. Raff, K. Roberts, and P. Walter. *Molecular Biology of the Cell*. Garland Science, New York, fourth edition, 2002.

[2] H. Antil, R. Glowinski, R. H. W. Hoppe, C. Linsenmann, T.-W. Pan, and A. Wixforth. Modeling, simulation, and optimization of surface acoustic wave driven microfluidic biochips. *J. Comp. Math*, 28:149–169, 2010.

[3] D. Bekah. Measurement of viscoelastic properties of treated and untreated cancer cells using passive microrheology. *(http://digitalcommons.ryerson.cy/dissertations/563)*, 2010.

[4] K. Bester. Chiral analysis for environmental applications. *Analytical and Bioanalytical Chemistry*, 376(3):302–304, 2003.

[5] R.P. Beyer. A computational model of the cochlea using the immersed boundary method. *Journal of Computational Physics*, 98:145–162, 1992.

[6] D. Boffi, N. Cavallini, and L. Gastaldi. Finite element approach to immersed boundary method with different fluid and solid densities. *Math. Models and Methods in App. Sciences*, 21:2523–2550, 2011.

[7] D. Boffi and L. Gastaldi. A finite element approach for the immersed boundary method. *Computers and Structures*, 81:491–501, 2003.

[8] D. Boffi, L. Gastaldi, and L. Heltai. Numerical stability of the finite element immersed boundary method. *Math. Mod. Meth. Appl. Sci.*, 17:1479–1505, 2007.

[9] D. Boffi, L. Gastaldi, and L. Heltai. On the CFL condition for the finite element immersed boundary method. *Computers and Structures*, 85:775–783, 2007.

[10] S. Burger, T. Franke, T. Fraunholz, R. Hoppe, M.A. Peter, and A. Wixforth. Numerical simulation of surface acoustic wave actuated separation of rigid enantiomers by the fictitious domain Lagrange multiplier method. *submitted*.

[11] K.A. Busch and M.A. Busch. *Chiral Analysis*. Elsevier, Amsterdam, 2006.

[12] J.L. Carey, J.P. McCoy, and D.F. Keren. *Flow Cytometry in Clinical Diagnostics*. ASCP Press, Chicago, fourth edition, 2007.

[13] A.N. Collins, G. Sheldrake, and J. Crosby (eds.). *Chirality in Industry: The Commerical Manufacture and Applications of Optically Active Compounds*. Wiley, Chichester, 1995.

[14] A.N. Collins, G. Sheldrake, and J. Crosby (eds.). *Chirality in Industry II: The Commerical Manufacture and Applications of Optically Active Compounds*. Wiley, Chichester, 1997.

[15] E. Eisenstein. Cell sorting: divide and conquer. *Nature*, 441(7097):1179–1185, 2006.

[16] L.J. Fauci and C.S. Peskin. A computational model of aquatic animal locomotion. *Journal of Computational Physics*, 77:85–108, 1988.

[17] A.L. Fogelson. A mathematical model and numerical method for studying platelet adhesion and aggregation during blood clotting. *Journal of Computational Physics*, 56:111–134, 1984.

[18] A.L. Fogelson and C.S. Peskin. A fast numerical method for solving the three-dimensional Stokes' equations in the presence of suspended particles. *Journal of Computational Physics*, 79:50–69, 1988.

[19] E. Francotte and W. Lindner (eds.). *Chirality in Drug Research*. Wiley-VCH, Weinheim, 2006.

[20] T. Franke, S. Braunmüller, L. Schmid, A. Wixforth, and D.A. Weitz. Surface acoustic wave actuated cell sorting (SAWACS). *Lab on a chip*, 6:789–94, 2010.

[21] T. Franke, R. Hoppe, C. Linsenmann, and K. Zeleke. Numerical simulation of surface acoustic wave actuated cell sorting. *To appear in Central European Journal of Mathematics*.

[22] T. Franke, R.H. W. Hoppe, C. Linsenmann, L. Schmid, C. Willbold, and A. Wixforth. Numerical simulation of the motion of red blood cells and vesicles in microfluidic flows. *Comp. and Vis. in Sc.*, 14:167–180, 2011.

[23] G.P. Galdi. An introduction to the Navier-Stokes initial-boundary value problem. *Advances in Mathematical Fluid Mechanics*, 1:1–98, 2000.

[24] A. Gantener, R.H.W. Hoppe, D. Köster, K. Siebert, and A. Wixforth. Numerical simulation of piezoelectrically agitated surface acoustic waves on microfluidic biochips. *Compu. Visual. Sci.*, 10:145–161, 2007.

[25] R. Glowinski. *Finite Element Methods for Incompressible Viscous Fluids. In Handbook of Numerical Analysis, Vol. IX, Ciarlet & J.L. Lions, eds.* North-Holland, Amsterdam, 2003.

[26] R. Glowinski, T.-W. Pan, T.I. Hesla, D.D. Joseph, and J. Periaux. A fictitious domain approach to the direct numerical simulation of incompressible viscous flow past moving rigid bodies: Application to particulate flow. *J. Comput. Phys*, 169:363–427, 2001.

[27] M.D. Gunzburger. *Finite Element Methods for Incompressible Viscous Flows: A Guide to Theory, Practice and Algorithms.* Academic Press, Boston, 1989.

[28] T.S. Hawley and R.G. Hawley. *Flow Cytometry Protocols*, volume 263. Humana Press, Totowa, NJ, second edition, 2004.

[29] R.H.W. Hoppe, C. Linsenmann, and K. Zeleke. Numerical simulation of surface acoustic wave actuated enantiomer separation by finite element immersed boundary method. *Submitted.*

[30] D. Köster. Numerical simulation of acoustic streaming on SAW-driven biochips. *SIAM J. Comp. Sci.*, 29:2352–2380, 2007.

[31] M. Kostur, M. Schindler, P. Talkner, and P. Hänggi. Chiral separation in microflows. *Physical Review Letters*, 96, 2006.

[32] N. Kurihara and J. Miyamoto (eds.). *Chirality in Agrochemicals.* Wiley, Chichester, 1998.

[33] O.A. Ladyzhenskaya. *The Mathematical theory of viscous incompressible flow.* Gordon and Breach, New York, 19663.

[34] P.C.H. Li. *Microfluidic Lab-on-a-Chip for Chemical and Biological Analysis and Discovery.* CRC Press, Boca Raton, 2006.

[35] Y. Liu and W. K. Liu. Rheology of red blood cell aggregation by computer simulation. *J. Comput. Phys.*, 220:139–154, 2006.

[36] Marcos, H.C. Fu, T.R. Power, and R. Stocker. Separation of microscale chiral objects by shear flow. *Physical Review Letters*, 102:158103–1 –158103–4, 2009.

[37] N. Pamme. Continuous flow separation in microfluidic devices. *Lab on a chip*, 7:1644–1657, 2007.

[38] R.N Patel (ed.). *Stereoselective Biocatalysis*. CRC Press, Boca Raton, 2000.

[39] C.S. Peskin. Flow patterns around heart valves: a digital computer method for solving the equations of motion. PhD thesis. *Physiol., Albert Einstein Coll. Med., Univ. Microfilms*, 378, 1972.

[40] C.S. Peskin. Numerical analysis of blood flow in the heart. *Journal of Computational Physics*, 25:220–252, 1977.

[41] C.S. Peskin. The immersed boundary method. *Acta Numerica*, 11:479–517, 2002.

[42] M.E. Roser. A three-dimensional computer model for fluid flow through a collapsible tube. *Ph.D. thesis, New York University*, 1994.

[43] H.M. Shapiro. *Practical Flow Cytometry*. Wiley-Liss, New York, fourth edition, 2003.

[44] R. Skalak and S. Chien. *Handbook of Bioengineering*. McGraw-Hill, New York, 1987.

[45] L.A. Sklar. *Flow Cytometry for Biotechnology*. Oxford University Press, New York, 2005.

[46] L. Tartar. *Introduction to Sobolev Spaces and Interpolation Theory*. Springer, Berlin-Heidelberg-New York, 2007.

[47] R. Temama. *Navier-Stokes equations: theory and numerical analysis*. AMS Chelsea publishing, 2000.

[48] K. Tsubota, S. Wada, and T. Yamaguchi. Simulation study on effects of hematocrit on blood flow properties using particle method. *J. Biomech. Sci. Eng.*, 1:159170, 2006.

[49] T. Wang, T.-W. Pan, Z.W. Xing, and R. Glowinski. Numerical simulation of red blood cell rouleaux in microchannels. *Phys. Rev. E*, 79:041916–1 – 041916–11, 2009.